



The Green Bank 820 MHz Pulsar Survey. I. Survey Overview and Initial Results

A. E. McEwen^{1,2}, R. S. Lynch³, D. L. Kaplan², C. Bolda^{2,4}, R. Sengar², E. Fonseca^{5,6}, T. Agoudeomos², J. Boyles⁷, S. Chatterjee⁸, T. Cohen⁹, F. Crawford¹⁰, M. E. DeCesar^{11,28}, A. Ehlke², T. Fernandez², E. C. Ferrara¹², W. Fiore^{5,6}, N. Gilhaus², M. Gleiter², J. W. T. Hessels^{13,14}, T. Holman², A. Joy², V. Kaspi¹⁵, V. Kondratiev¹⁴, H. D. Leon², L. Levin¹⁶, B. Lorenz², D. R. Lorimer^{5,6}, D. R. Madison¹⁷, M. A. McLaughlin^{5,6}, B. W. Meyers^{18,19}, E. Parent^{20,21}, L. Patron², S. M. Ransom²², P. S. Ray²³, M. S. Roberts²⁴, S. Roch², X. Siemens²⁵, G. Stearns², J. K. Swiggum^{2,26}, I. H. Stairs¹⁹, K. Stovall²⁷, C. M. Tan¹⁵, N. Valentine², and J. van Leeuwen¹⁴

¹ Department of Physics, The George Washington University, Washington, DC 20052, USA; alexander.mcewen@nanograv.org

² Center for Gravitation, Cosmology, and Astrophysics, Department of Physics, University of Wisconsin-Milwaukee, P.O. Box 413, Milwaukee, WI 53201, USA

³ Green Bank Observatory, P.O. Box 2, Green Bank, WV 24494, USA

⁴ Department of Physics and Astronomy, Texas A&M University, College Station, TX 77845, USA

⁵ Department of Physics and Astronomy, West Virginia University, P.O. Box 6315, Morgantown, WV 26506, USA

⁶ Center for Gravitational Waves and Cosmology, West Virginia University, Chestnut Ridge Research Building, Morgantown, WV 26505, USA

⁷ Department of Physics and Astronomy, Western Kentucky University, 1906 College Heights Boulevard, Bowling Green, KY 42101, USA

⁸ Cornell Center for Astrophysics and Planetary Science and Department of Astronomy, Cornell University, Ithaca, NY 14853, USA

⁹ Department of Physics, New Mexico Institute of Mining and Technology, 801 Leroy Place, Socorro, NM 87801, USA

¹⁰ Department of Physics and Astronomy, Franklin & Marshall College, P.O. Box 3003, Lancaster, PA 17604, USA

¹¹ George Mason University, Fairfax, VA 22030, USA

¹² Department of Astronomy, University of Maryland, College Park, MD 20742, USA

¹³ Anton Pannekoek Institute for Astronomy, University of Amsterdam, Science Park 904, 1098 XH Amsterdam, The Netherlands

¹⁴ ASTRON, Netherlands Institute for Radio Astronomy, Oude Hoogeveensedijk 4, 7991 PD Dwingeloo, The Netherlands

¹⁵ Department of Physics & McGill Space Institute, McGill University 3600 University Street, Montreal, QC H3A 2T8, Canada

¹⁶ Jodrell Bank Centre for Astrophysics, School of Physics and Astronomy, University of Manchester, Manchester M13 9PL, UK

¹⁷ Department of Physics, University of the Pacific, 3601 Pacific Avenue, Stockton, CA 95211, USA

¹⁸ International Centre for Radio Astronomy Research (ICRAR), Curtin University, Bentley, WA 6102 Australia

¹⁹ Department of Physics and Astronomy, University of British Columbia, 6224 Agricultural Road, Vancouver, BC V6T 1Z1 Canada

²⁰ Institute of Space Sciences (ICE, CSIC), Campus UAB, Carrer de Can Magrans s/n, E-08193 Barcelona, Spain

²¹ Institut d'Estudis Espacials de Catalunya (IEEC), Carrer Gran Capità 2-4, E-08034 Barcelona, Spain

²² National Radio Astronomy Observatory, 520 Edgemont Road, Charlottesville, VA 22903, USA

²³ U.S. Naval Research Laboratory, Washington, DC 20375, USA

²⁴ Eureka Scientific, Oakland, CA, USA

²⁵ Department of Physics, Oregon State University, Corvallis, OR 97331, USA

²⁶ Department of Physics, 730 High St., Lafayette College, Easton, PA 18042, USA

²⁷ National Radio Astronomy Observatory, 1003 Lopezville Road, Socorro, NM 87801, USA

Received 2024 January 18; revised 2024 April 29; accepted 2024 May 2; published 2024 July 5

Abstract

The Green Bank 820 MHz pulsar survey covers $\simeq 173$ deg² in the Cygnus X region of the Galaxy, centered on $l = 84.5$ and $b = 1.5$. Significant star formation is present in this region, and lines of sight pass through three arms of the Galaxy (Orion–Cygnus, Perseus, and an outer arm). Using the Green Bank Telescope, we recorded 200 MHz of bandwidth for 4.5 minutes at 81.92 μ s resolution for each of 3457 observed survey pointings during 2016 and 2017, covering about two-thirds of the total area. We searched these data for pulsars and report the discovery of six new pulsars—PSRs J2016+3820, J2016+4231, J2019+3810, J2035+3538, J2035+3655, and J2041+4551—and the codiscovery of PSR J2057+4701. PSR J2035+3655 is in a short (4.5 hr) binary orbit; we report the full binary solution and weakly constrain the mass of the pulsar via a marginal (2σ) detection of the Shapiro delay. We also searched the survey data for known pulsars to estimate the survey's sensitivity and measured 820 MHz pulse widths and flux density for 20 detected sources. For sources that were also detected in the Green Bank North Celestial Cap survey at 350 MHz, we measure scattering parameters and compare to expectations for the region. With these results, we revisit the population estimates that motivated this survey and consider the impact of the survey's yield on their underlying models. We note an apparent underestimate in dispersion measure predictions from typical Galactic electron density models in the survey region, and discuss future observation strategies.

Unified Astronomy Thesaurus concepts: [Radio pulsars \(1353\)](#); [Radio astronomy \(1338\)](#); [Surveys \(1671\)](#)

1. Introduction

As our understanding of the physical laws that provide the scaffolding for the Universe improves, laboratories for further study continue to evolve toward the exotic and uncommon. Pulsars are excellent subjects for many such extreme experiments, as their rotational stability (e.g., Verbiest et al. 2009) makes them unmatched tools for tracking time across Galactic distances. They probe extreme gravity almost as much

²⁸ Resident at the U.S. Naval Research Laboratory, Washington, DC 20375, USA.

as black holes, but with the advantage of direct observational signatures. This makes them suitable subjects for a host of gravitation experiments, ranging from individual mass measurements and neutron star equation of state constraints (Özel & Freire 2016; Cromartie et al. 2020; Agazie et al. 2021), to measurements of gravitational waves from supermassive black hole binaries (both as individual sources; i.e., Babak et al. 2016; Aggarwal et al. 2019; Arzoumanian et al. 2023; and as a stochastic background of all sources; i.e., Shannon et al. 2013; Lentati et al. 2015; Arzoumanian et al. 2020), and for detailed descriptions of the distribution of matter in the interstellar medium (ISM; Turner et al. 2021; Wahl et al. 2022).

This potential for extreme science is only limited by the number of sources available for study. To date, there are >3300 pulsars listed in version 1.7 of the ATNF catalog²⁹ (Manchester et al. 2005). These sources range more than 3 orders of magnitude in period and dispersion measure (DM), and include nearly 400 binary systems. However, population models predict tens of thousands more pulsars in the Galaxy beamed toward Earth yet to be discovered, if only we know where (and how) to look (Swiggum et al. 2014; Venkatraman Krishnan et al. 2020; Sengar et al. 2023; Zhou et al. 2023; Dong et al. 2023). Every new pulsar provides an opportunity for improving our understanding of the population. Pulsar searching is crucial for expanding this population, and for continuing the exploration of new scientific avenues (Hallinan et al. 2019; Lynch et al. 2019; Ransom et al. 2019).

In this paper, we describe the observations and results of a sensitive pulsar survey with the Green Bank Telescope (GBT) conducted at a central frequency of 820 MHz. The survey, hereafter referred to as GBT820, is motivated in Section 2. Observations and data reduction are described in Section 3, and follow-up observations of new discoveries are given in Section 4. The newly discovered pulsars are detailed in Section 5. In Section 6, we discuss the implications of our results. Finally, in Section 7, we present our conclusions.

2. Survey Motivation and Overview

The rate of pulsar discovery has remained remarkably constant (about 100 new pulsars published each year) over the past two decades. This is owing to a number of surveys that cover vast regions of the sky (Manchester et al. 2001; Stovall et al. 2014; Sanidas et al. 2019; Cameron et al. 2020) and are complemented by smaller, deeper searches in regions of particular interest (Ridley et al. 2013; Titus et al. 2019; Hisano et al. 2022). Both strategies have been successful, and both are necessary to understand the underlying pulsar population. These searches are made more efficient with ever improving sensitivity limits provided by new instruments (Braun et al. 2019; Jiang et al. 2019; Gautam et al. 2022) and candidate sifting techniques (Karako-Argaman et al. 2020; Yu et al. 2020; Sengar et al. 2023).

The Cygnus region observed in this work is known to harbor many sites of star formation, including extensive OB associations (Comerón & Pasquali 2012; Berlanas et al. 2019; Quintana & Wright 2021; Orellana et al. 2021; Quintana & Wright 2022), Wolf-Rayet (W-R) stars (Koch-Miramond et al. 2002; Rauw et al. 2015), and H II regions (Beerer et al. 2010; Emig et al. 2022). As such, it has been invaluable for studying the entire life cycle of stars—many of which have

formed within the past few million years (van der Walt et al. 2021; Beuther et al. 2022). Many of these studies have focused on the relatively nearby (≈ 1.4 kpc; Rygl et al. 2012; Orellana et al. 2021) star-forming region along this line of sight, known as Cygnus X (Piddington & Minnett 1952). Beyond it lie two more Galactic arms, one of which is home to the extensively studied source Cygnus X-3, a microquasar in a binary with a W-R star that exhibits both X-ray and radio emission (Trushkin et al. 2017; Broderick et al. 2021; Suryanarayanan et al. 2022; McCollough et al. 2022). These studies illuminate a rich stellar history in the Cygnus region, making it a prime target for pulsar surveys since pulsars are formed during the supernovae of massive stars.

Despite this, there have not been many searches for pulsars in this region, and they have not covered a particularly wide range of radio frequencies. At the time that this study began, 15 radio pulsars had been previously identified in the GBT820 region (Davies & Large 1970; Davies et al. 1973; Stokes et al. 1985; Dewey et al. 1985; Sayer et al. 1996; Roberts et al. 2002; Hessels et al. 2008; Janssen et al. 2009; Abdo et al. 2009; Arzoumanian et al. 2011; Camilo et al. 2012; Berezhina et al. 2017). Given that these sources were identified primarily in low radio frequency surveys (< 400 MHz; Stokes et al. 1985; Dewey et al. 1985; Hessels et al. 2008), it was hypothesized that the dense regions of material here may hamper low radio frequency detection of pulsars with higher DMs because of scattering and dispersion. The High Time Resolution Universe survey (Keith et al. 2010) is one high-frequency (1.4 GHz) survey that covered Cygnus, but no new pulsars were detected. Observing frequencies above 1 GHz are not as strongly sensitive to the deleterious scattering/dispersion effects, so an explanation for the dearth of pulsars is likely related to the lower luminosity of radio pulsars at higher frequencies that results from their steep (negative) spectral indices.

The GBT820 survey was designed to strike a balance between these two regimes, opting for a midrange observing frequency of 820 MHz. The average DM of the known pulsars in Cygnus is ≈ 195 pc cm⁻³; the maximum DMs predicted by the Galactic electron density models YMW+16 (Yao et al. 2017) and NE2001 (Cordes & Lazio 2002) reach as high as 500 pc cm⁻³, and several recent discoveries significantly exceed these predictions (e.g., PSRs J2030+3944g and J2021+4024g with respective DMs of 937.4 and 680.5 pc cm⁻³; Han et al. 2021). Compared to observing at 400 MHz, intrachannel dispersion smearing for such a source is reduced by a factor of ≈ 25 (per Equation (5.2) in Lorimer & Kramer 2012). Assuming a mean spectral index for pulsar emission of -1.4 (Bates et al. 2014), pulsars observed at 820 MHz will be about 2.1 times brighter (on average) than they would appear in a comparable scan at 1400 MHz. Using measurements of flux density at both 820 MHz and 1400 MHz from the ATNF catalog (v1.71), approximately 90% of pulsars are brighter at 820 MHz. Thus, GBT820 was conceived to find young pulsars buried in the Cygnus region.

3. Observations and Data Reduction

Observations were conducted during the semesters of 2016A and 2017A (project code GBT16A-349, PI: R. Lynch). The region of interest was divided into 4752 grid points covering the region of $75^\circ \leq l \leq 94^\circ$, $-3^\circ \leq b \leq 6^\circ.1$ (172.9 deg²), though only 3457 (73%) of these were actually observed; the unobserved region includes all points with decl. $> 48^\circ.5$. Due to

²⁹ <https://www.atnf.csiro.au/research/pulsar/psrcat/>

Table 1
Overview of the Survey Parameters

Parameter	Value/Range
Galactic Latitude, b (deg)	[−3, 6.1]
Galactic Longitude, l (deg)	[75, 94]
Sky Area (deg ²)	172.9
$N_{\text{obs}}/N_{\text{surv}}$	3457/4752
Center Frequency, ν (MHz)	820
Bandwidth, $\Delta\nu$ (MHz)	200
Dwell Time, T_{obs} (s)	270
Pulsars Discovered/Detected	6/20
Minimum Detected Flux Density, S_{min} (mJy)	0.08

Note. Aside from the observation setup and sky coverage, we include the number of pulsars detected/discovered in the survey and the minimum detected flux density. Note that the coordinates listed describe the full survey region—points with decl. above 48°5 have not been observed.

scheduling difficulties and the availability of other instruments for probing the Galactic plane that have come online since GBT820’s inception (i.e., the Five-hundred-meter Aperture Spherical Telescope (FAST), Jiang et al. 2019; the Canadian Hydrogen Intensity Mapping Experiment (CHIME), CHIME/Pulsar Collaboration et al 2021), the remainder of the survey is unlikely to be completed. However, the data that are available comprise a uniquely sensitive and uniform pulsar survey of the Cygnus region. The grid spacing was chosen such that adjacent points were separated by approximately 11.′2, or 80% of the beam half-width at half-maximum. Data were recorded with the Green Bank Ultimate Pulsar Processing Instrument (GUPPI) backend (DuPlain et al. 2008) and the GBT’s 820 MHz prime focus receiver, covering 200 MHz of bandwidth and an integration time of 4.5 minutes per pointing with 81.92 μs time resolution. The bandwidth was divided into 4096 channels to accurately correct for dispersive delays and to better mitigate radio frequency interference (RFI). We list the survey parameters in Table 1, and the survey region is shown in Figure 1.

3.1. PRESTO Processing

Following observations, data were processed on the Béluga supercomputer operated by the Digital Research Alliance of Canada.³⁰ Processing followed a pipeline similar to the one described in Stovall et al. (2014): raw data were cleaned using an automated RFI zapping scheme and `rfifind` in the PRESTO package (Ransom 2001) following a pipeline similar to that described in Stovall et al. (2014), dedispersed at 11,670 trial DMs ranging from 0 to 4096 pc cm^{-3} (intrachannel smearing ranging from $\approx 10^{-4}$ to 2.4 ms), and subsequently Fourier transformed. Resulting plots for DMs below 2 pc cm^{-3} were created for diagnostic checks, but were not searched. This step also included corrections for orbital acceleration (up to a PRESTO `zmax` value of 50, which corresponds to a maximum acceleration of 281 m s^{-2} for a pulsar with a 10 m s^{-1} spin period) to improve sensitivity to sources in binaries. Data that were dedispersed at higher DMs were downsampled to account for expected intrachannel dispersive smearing. Due to persistent RFI near 745 MHz and 885 MHz, we removed a total of 40 MHz from all data before processing, leaving 160 MHz of the survey bandwidth. Peaks in the resulting Fourier

spectra correspond to candidates; for each candidate period–DM combination, the dedispersed time series was divided into single-rotation pieces and these were summed in phase (a process called “folding”). To eliminate false positives caused by RFI and identify the most promising astrophysical signals, candidates were sifted based on their characteristics such as Fourier power, harmonic content, DM, etc. (see Stovall et al. 2014 for more details) to produce a final list of candidates. Diagnostic plots were produced for each of these candidates to be assessed by eye.

3.1.1. Periodic Candidates

Candidate signals that reached a significance threshold (6σ) in the Fourier spectrum of dedispersed data were folded using `prepfold` from the PRESTO package. This process produces descriptive plots that include temporal, spectral, and diagnostic information about the observation and candidate. Signals from data dedispersed with $\text{DM} \gtrsim 2 \text{ pc cm}^{-3}$ that persist in frequency and time at a given rotation phase indicate astrophysical, repeating sources, and therefore warrant follow-up observation. When pulsars are accelerated along the line of sight due to binary motion, the observed spin period will be modulated at the orbital period. This is not typically the case for short survey scans like the ones used in GBT820. More common are orbits with $P_{\text{orb}} \gg T_{\text{obs}}$, where this variation is limited to a small orbital phase range and is better approximated as a linear or quadratic drift in the pulsar’s period. To account for this motion (and search for such sources), we also implemented the `accelsearch` routine from PRESTO, which searches over a specified range of pulsar accelerations to produce appropriately Doppler-shifted templates. These templates are then matched to the power spectra of the dedispersed time series. From the 3457 beams that were searched, 140,490 candidates were found and folded with `prepfold` for visual inspection.

3.2. PEASOUP Processing

Given the recent success in reprocessing pulsar surveys through optimized search and classification methodologies (e.g., Morello et al. 2019; Sengar et al. 2023), we processed the GBT820 data using pipeline and candidate classification approaches similar to those outlined in Sengar et al. (2023). The pipeline is built around a GPU-based pulsar search library PEASOUP, which uses a time-domain resampling algorithm (Johnston & Kulkarni 1991) to search for binary pulsars. Prior to processing the data, the `psrfits`-format files of the survey were first converted to `filterbank` format using the `digifil` tool of `dspsr` (van Straten & Bailes 2011).³¹ To expedite the data processing while preserving the original time resolution, we reduced the spectral resolution of the data down to 2048 frequency channels. Apart from this, given specific constraints in the storage capacity, we reduced the bit depth from 8 bit to 2 bit. This not only conserved storage space but also further enhanced the processing speed of the survey. Additionally, the choice of 2 bit data was motivated by its potential to introduce quantization noise which aids in suppressing certain types of RFI. While reducing the bit depth can lead to loss in sensitivity, for GBT820 data, this loss was found to be negligible. We confirmed this through a

³⁰ <https://docs.alliancecan.ca/wiki/Beluga/en>

³¹ <https://sourceforge.net/projects/dspsr/>

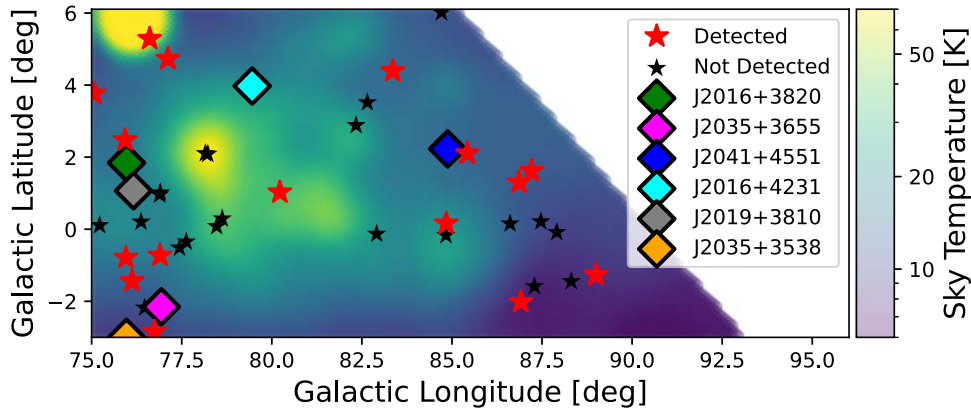


Figure 1. GBT820 survey observing coverage. We show a Galactic map of the observed region of the survey. Stars indicate pulsars (both from the ATNF catalog and from survey websites, as listed in Tables 2 and 3), and colors indicate whether the pulsar was detected. We also plot the new discoveries from the survey with diamonds. The background color reflects the sky temperature in the survey calculated from PyGDSM and scaled using a power law with spectral index -2.6 (Haslam et al. 1982). The bright source at $l = 76^\circ.2$, $b = +5^\circ.8$ is the radio galaxy Cygnus A ($S_{820 \text{ MHz}} \approx 3 \text{ kJy}$; Kellermann et al. 1969). The bright source at $l = 78^\circ.2$, $b = 2^\circ.1$ is the complex region containing the supernova remnant (SNR) G78.2+2.1 (γ Cygni).

comparison of the signal-to-noise ratios (S/Ns) of the known pulsars in the survey at different bit depths in which the loss in sensitivity was only 2%–3%.

We searched the GBT820 observations across a DM range extending from 2 to 1000 pc cm^{-3} , which resulted in 3718 trial DMs, and the acceleration range was $|a| = 250 \text{ m s}^{-2}$ with 40 trial accelerations. This pipeline is particularly sensitive to narrow duty cycle pulsars for which multiple harmonics are necessary for the peak detection.

Narrow periodic signals display power across various harmonics in the Fourier domain (Bracewell 2000). Therefore, to enhance the detection capabilities in the fast Fourier transform (FFT), it is advisable to incorporate as many harmonics as feasible. While standard pulsar searches typically sum up to 16 harmonics coherently (Ransom et al. 2002), both for faster computation and to limit the number of candidates produced, there is a potential drawback: faint narrow duty cycle pulsars might go undetected. Additionally, the incoherent summing of harmonics can further diminish the S/N in the spectral domain, making it even more challenging to identify these pulsars. Consequently, employing greater number of harmonics can increase the likelihood of a candidate appearing in the candidate list. Sengar et al. (2023) found that on average the folded S/Ns for such faint narrow duty cycle pulsars can be 1.5–2.0 times higher than their spectral S/Ns. This underscores the importance of folding candidates from the FFT noise floor, i.e., those with a spectral S/N (S/N_{FFT}) close to five, in order to effectively target faint narrow duty cycle pulsars. However, considering candidates for folding with such low S/N_{FFT} poses its own challenge. As we move forward towards fainter candidates, their number grows exponentially, making it impractical to fold all of them. Therefore, instead of relying on a fixed S/N_{FFT} cutoff, we adopted the candidate sifting criteria described in Sengar et al. (2023). This approach involves initially sifting based on spin period, S/N_{FFT} , as well as the number of harmonic sums (nh) corresponding to each candidate, allowing for comprehensive coverage and evaluation of the candidates. These criteria are as follows:

$$\text{For } P < 100 \text{ ms: } \begin{cases} P < 30 \text{ ms:} & \{S/N_{\text{FFT}} \geq 7.5, nh < 4, \\ 30 \text{ ms} < P < 100 \text{ ms:} & \{S/N_{\text{FFT}} \geq 7.0, nh \geq 1, \\ P < 100 \text{ ms:} & \{S/N_{\text{FFT}} \geq 9.5, nh = 0, \end{cases}$$

$$\text{For } P > 100 \text{ ms: } \begin{cases} P > 100 \text{ ms:} & \begin{cases} S/N_{\text{FFT}} \geq 7.0, nh \geq 1, \\ S/N_{\text{FFT}} \geq 10, nh = 0, \end{cases} \\ P \geq 200 \text{ ms:} & \{5.5 \leq S/N_{\text{FFT}} \leq 7.0, nh \geq 2. \end{cases}$$

Employing the candidate sifting criteria mentioned above, out of $\sim 15,000$ candidates per observation from the PEASOUP pipeline candidate list, on average 600 candidates per observation successfully passed through the selection process, as depicted in Figure 2(b). These retained candidates underwent folding using `dspsr` to create folded archive files which were cleaned using `clfd`³² (Morello et al. 2019). The folded diagnostic plots were generated using the `pdmp` module of PSRCHIVE. Given the substantial number of folded diagnostic plots, we used the filtering method described in Sengar et al. (2023), which uses the candidate’s folded profile parameters to determine whether a candidate should be visually inspected or not. In this method, during the first round of candidate rejection, those with optimized DM values $< 2 \text{ pc cm}^{-3}$ (to eliminate terrestrial signals) and/or folded S/N below 8.5 were eliminated, as demonstrated in Figure 2(c). The remaining candidates were subject to further refinement through the determination of β (the difference of the optimized DM and the DM determined by the FFT, normalized by the FFT DM), γ (ratio of the optimal DM’s error and the DM value), and η (ratio of the DM = 0 pulse S/N and the S/N measured at the optimal DM) factors. For more details on these factors, see Section 3.1.3 of Sengar et al. (2023). This additional step significantly reduced the candidate pool, as shown in Figure 2(d). Overall from 90% of the survey processed, about 8000 diagnostic plots were visually inspected.

4. Candidate Inspection and Follow-up

Candidates from the survey pipelines were visually inspected following the automatic folding. When an astrophysical candidate was identified, provisional ephemerides based on the discovery position, DM, and spin frequency of the candidate were used to attempt to detect the sources with CHIME (400 MHz of bandwidth centered on 600 MHz; CHIME/Pulsar Collaboration et al 2021). To compare the sensitivity of the two instrumental setups, we can compare the

³² <https://github.com/v-morello/clfd>

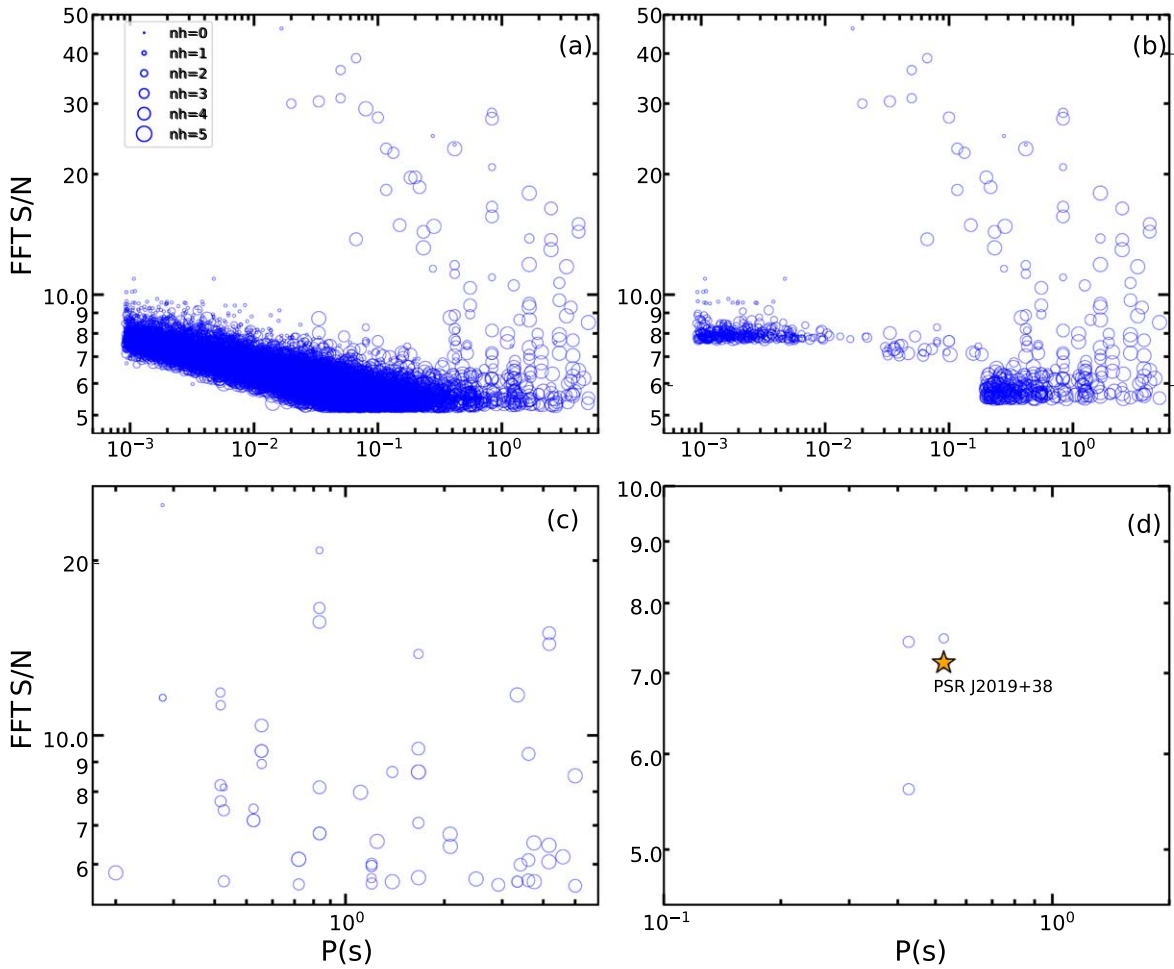


Figure 2. An example of the candidate discerning criteria used in the reprocessing of the GBT820 survey. We show the distribution in terms of their spin period and spectral S/N (S/N_{FFT}). The size of the data points is scaled proportionally according to the number of harmonics (nh) summed in generating the candidate. Panel (a) shows all candidates produced in one of the observations in which a new pulsar, PSR J2019+38, was detected. Panel (b) showcases the candidates that were selected for folding. Panel (c) represents the candidates that survived after the first iteration of rejection. Panel (d) showcases that only four candidates survived the final classification criteria and were visually inspected.

minimum predicted flux density detectable in a given observation with both telescopes. We use published mean system equivalent flux densities for both CHIME (55 Jy; Merryfield et al. 2023) and the GBT (15 Jy, from the GBT proposer’s handbook³³). Because CHIME is a transit telescope, the gain and observation duration are dependent on decl. This makes predictions somewhat more complex; for simplicity, we assume an average duration of about 15 minutes and an average effective bandwidth of 300 MHz to account for RFI. With these factors in mind, using the radiometer equation as described in Lorimer & Kramer (2012), we expect that the ratio of minimum flux densities measurable in a GBT820 survey scan to a CHIME confirmation scan to be approximately 0.95. In practice, this will depend on the exact sky temperature, how scattered the pulsar is, details of the observation and RFI mitigation, etc. Despite this loss in sensitivity for a single observation, the availability of daily cadence with CHIME allows for multiple observations to be summed in short order, greatly increasing the total observation duration. Still, nondetections with CHIME are less conclusive than those made with the GBT, which has better sensitivity, and were

followed up with GBT observations as is described in Section 5.

4.1. Known Pulsars

Per version 1.7 of the ATNF catalog, 32 pulsars are in the observed region of the survey. There are also sources which are not included in the catalog, but are posted as discoveries on survey websites that are linked in Tables 2 and 3 and were compiled using the pulsar survey scraper (Kaplan 2022). In total, 46 are in the region where observations have been completed, and 23 are detected in these data. For these pulsars, we measure pulse widths and flux densities at 820 MHz using the most significant detection. To quantify this, we define the S/N

$$S/N = \sum_i \frac{p_i - \bar{p}_{\text{off}}}{\sigma_{\text{off}} \sqrt{W_b}}, \quad (1)$$

where p_i is the intensity as measured in a given phase bin, \bar{p}_{off} and σ_{off} are the mean and standard deviation of the off-pulse bins, respectively, and W_b is the pulse window in phase bins. Note that this width differs slightly from the widths reported in Table 2 (W_{50} and W_{10}), as W_b indicates the number of bins where the pulse is visible. For the measurements of W_{50} and

³³ <https://www.gb.nrao.edu/scienceDocs/GBTpg.pdf>

Table 2

Flux Densities and Pulse Widths for Known Pulsars Detected in the GBT820 Survey, Split into Groups of GBT820 Discoveries and Other Known Sources

PSR	S/N	S_{820} (mJy)	W_{50} (ms)	W_{10} (ms)
Survey Discoveries				
J2016+3820	10(3)	0.29(10)	9.842(4)	26.137(4)
J2016+4231	9(5)	0.12(7)	29(9)	78(9)
J2019+3810	7(4)	0.09(6)	24(4)	41(4)
J2035+3538	9(4)	0.07(4)	7(4)	45(4)
J2035+3655	12(3)	0.44(13)	0.6840(4)	3.0770(4)
J2041+4551	30(4)	1.1(2)	45.17(2)	180.12(2)
J2057+4701*	13(4)	0.28(11)	8.267(9)	22.602(9)
Known Sources				
J2002+4050	235(12)	7(2)	17.5(2)	51.34(5)
J2005+38 ^a	7(5)	0.17(13)	102.18(4)	109.61(4)
J2006+4058	36(15)	0.9(4)	18.216(8)	22.373(8)
J2013+3845	191(5)	9(2)	15.28(13)	28.3(2)
J2026+3656g ^b	4(5)	0.08(9)	27.27(3)	79.62(3)
J2027+4557	164(6)	6(2)	19.7(4)	68.3(8)
J2029+3744	105(8)	3.2(8)	19.9(4)	38.8(8)
J2030+3641	19(3)	0.8(3)	9(3)	17(4)
J2032+4127	12(4)	0.6(2)	6.8(4)	12.29(12)
J2037+3621	145(7)	3.7(11)	12.6(11)	35.2(11)
J2044+4614	80(4)	26.2(9)	26.2(9)	121(13)
J2051+4434g	16(2)	0.6(2)	229.81(2)	378.36(2)
J2053+4650	51(2)	2.6(6)	1.4010(2)	3.4940(2)
J2053+4718	29(3)	1.5(4)	52.25(8)	167.07(8)
J2108+4441	371(7)	14(5)	24.1(5)	37.3(4)
J2113+4644	675(7)	36(12)	60.5(15)	203(2)

Notes. Searches through other surveys were done using the pulsar survey scraper (Kaplan 2022). Uncertainties in parentheses are 1σ on the last digit. The asterisk in the first column denotes the codiscovery of J2057+4701 with Dong et al. (2023), and superscripts indicate pulsars discovered in other surveys that have not yet been published.

^a Listed on the CHIME/Pulsar (CHIME/Pulsar Collaboration et al 2021) Discovery page: <http://catalog.chime-frb.ca/galactic>

^b Listed on the FAST-GPPS (Han et al. 2021) Discovery page: <http://zmtt.bao.ac.cn/GPPS/GPPSnewPSR.html>

W_{10} , we first identify W_b by flattening the profile (removal of a polynomial fit to the off-pulse region; this eliminates additional RFI and red noise contamination) and choosing a window that includes all phase bins above the mean off-pulse noise. We then find where in this window the profile drops below 50% and 10% of the pulse maximum, respectively.

Using the S/N measured above, we can translate to pulsar flux density using the radiometer equation (see, e.g., Lorimer & Kramer 2012) which gives the flux density at 820 MHz

$$S_{820} = \beta \frac{(S/N)T_{\text{sys}}}{G\sqrt{np}t_{\text{int}}\gamma\Delta\nu} \sqrt{\frac{W}{P - W}}. \quad (2)$$

In this expression, $\beta = 1.1$ is a correction factor to account for 8 bit data digitization in GUPPI (Lorimer & Kramer 2012), $T_{\text{sys}} = T_{\text{sky}} + T_{\text{rec}} + T_{\text{CMB}}$ is the sum of sky, receiver, and cosmic microwave background (CMB) temperatures, $G = 2 \text{ K Jy}^{-1}$ is the gain of the GBT, $np = 2$ is the number of summed polarizations, $t_{\text{int}} = 4.5$ minutes is the observation duration, $\Delta\nu = 200 \text{ MHz}$ is the full bandwidth that is adjusted by the fraction of used/total bandwidth γ , W is the pulse width, and P

Table 3

Nondetections of known Pulsars in GBT820

PSR	Explanation	S_{820} Upper Limit [μJy]	Reference
J2001+4209g	single pulse source	...	Zhou et al. (2023)
J2021+3651	below sensitivity	86	Roberts et al. (2002), Abdo et al. (2009)
J2021+4024g	below sensitivity	122	Han et al. (2021)
J2021+4026	gamma-ray pulsar	...	Trepl et al. (2010), Ray et al. (2011)
J2022+3842	scattered X-ray pulsar	...	Arzoumanian et al. (2011)
J2022+3845g	below sensitivity	129	Han et al. (2021)
J2024+3751g	below sensitivity	90	FAST Discovery ^a
J2024+48	updated position	...	Hessels et al. (2008)
J2029+4453g	below sensitivity	88	FAST Discovery ^a
J2030+3818g	below sensitivity	120	Han et al. (2021)
J2030+3833g	single pulse source	...	Zhou et al. (2023)
J2030+3929g	below sensitivity	116	Han et al. (2021)
J2030+3944g	below sensitivity	116	Han et al. (2021)
J2030+4415	gamma-ray pulsar	...	Pletsch et al. (2012)
J2034+3632	gamma-ray pulsar	...	Fermi-LAT ^b
J2042+4550g	below sensitivity	78	FAST Discovery ^a
J2046+4253g	below sensitivity	92	FAST Discovery ^a
J2052+4421g	below sensitivity	73	Han et al. (2021)
J2058+4555g	below sensitivity	71	FAST Discovery ^a
J2101+4636g	below sensitivity	72	FAST Discovery ^a
J2104+4644g	below sensitivity	70	FAST Discovery ^a
J2108+4516	scattered binary system	71	Good et al. (2021)
J2111+4606	gamma-ray pulsar	...	Pletsch et al. (2012)

Notes.

^a Listed on the FAST-GPPS Discovery page: <http://zmtt.bao.ac.cn/GPPS/GPPSnewPSR.html>

^b Listed on the Fermi Large Area Telescope (LAT) Discovery page: https://einsteinathome.org/gammaraypulsar/FGPR1_discoveries.html

is the pulse period. Sky temperatures in the survey region (calculated using `PyGDSM`; Price 2016³⁴) are mostly in the range of 8–50 K at the survey’s central frequency (820 MHz), though some points exceed 300 K. Manual excision removed 20% of bandwidth for all beams, along with automatic RFI mitigation with `rfifind` (masking at most 10% of the remaining band); the mean unmasked fraction for the survey is $\gamma = 0.79$.

In most cases, the pulsars were detected in multiple nearby survey beams; for the brightest pulsars, this is as many as 10 beams. For all analyses, we use the detection with the highest S/N. These measurements are presented in Table 2, and all pulsars in the survey region are shown in Figure 1. These pulsars are also presented in the $P - \dot{P}$ diagram in Figure 3, with survey discoveries, detections, and nondetections highlighted.

We examined the 23 missed pulsars to explain their nondetections, and in all cases, the nondetections are not

³⁴ <https://github.com/telegraphic/pygdsmtree/master>, which uses an updated Haslam et al. (1982) map developed in Remazeilles et al. (2015) with a spectral index of -2.6 .

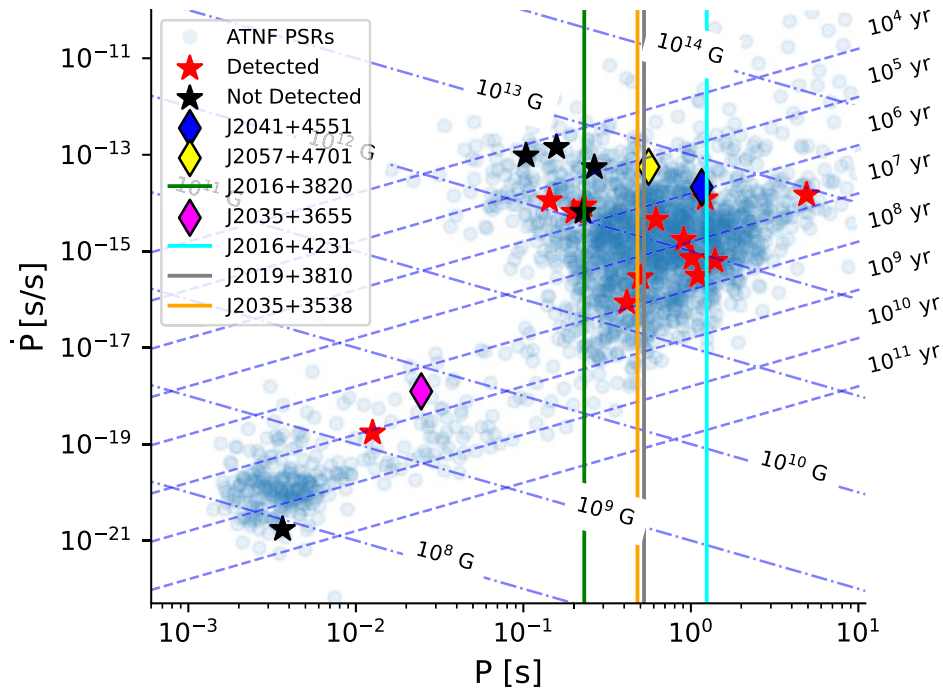


Figure 3. $P - \dot{P}$ diagram of pulsars, highlighting those discovered by this survey. Stars indicate pulsars from the ATNF catalog in our survey region, and colors indicate whether the pulsar was detected. We also include the remaining pulsars in the ATNF catalog as blue circles. Due to the lack of a constraint on \dot{P} for discovery PSRs J2016+3820, J2016+4231, J2019+3810, and J2035+3538, we include vertical lines at their discovery periods.

surprising. As a check, each survey point covering these sources were manually checked using their (known) ephemerides; none were detected. Many of these pulsars have large DMs (only three of the missed sources have $DM < 250 \text{ pc cm}^{-3}$), and have been discovered in surveys using FAST at frequencies $\geq 1 \text{ GHz}$ (e.g., J2021+4024g, J2022+3845g, and J2052+4421g; Han et al. 2021, and others listed on the FAST-GPPS website), where scattering has less of an impact and fainter pulsars are still above the telescope’s sensitivity limit. The pulse profiles for these three sources (available on the survey’s website³⁵) show visible scattering at 1.25 GHz, suggesting that this effect is likely degrading their S/Ns substantially at 820 MHz. Additionally, flux densities measured at 1.25 GHz have been published (88 μJy , 55 μJy , and 280 μJy , respectively; Han et al. 2021); assuming a common spectral index of -1.4 (Bates et al. 2013) and typical scatter broadening (Bhat et al. 2004), emission from these sources (approximately 159, 99, and 505 μJy) is very close to (or above) the limiting flux density we predict in this survey ($>10^4$, 272, and 486 μJy) for their DMs (681, 488, and 547 pc cm^{-3}). Also among the missed detections are a few pulsars discovered via high-energy emission, many of which appear to be radio quiet (or at least too faint in radio for this search). Missed detections are included with explanations and references in Table 3. For sources with previously measured periods, DMs, and flux densities (at other frequencies) we include 3σ upper limits on their flux density at 820 MHz. To estimate these, approximate scattering and DM smearing timescales are drawn from the results of Bhat et al. (2004), intrinsic pulse widths are taken to be 6% of the pulse period, and we incorporate the masking information for the nearest beam to each missed pulsar.

J2024+48 was originally discovered at 350 MHz (GBT350 survey; Hessels et al. 2008) and has a relatively long period

(1.2 s) and low DM (99 pc cm^{-3}), initially making its nondetection puzzling. However, subsequent observations have determined an improved position for this pulsar which places it outside of the GBT820 survey area (Jason Hessels, private communication).

5. Discoveries

The GBT820 survey has discovered and confirmed six new pulsars: J2016+3820, J2016+4231, J2019+3810, J2035+3538, J2035+3655, and J2041+4551. Another source, J2057+4701, was identified in GBT820 data in 2022 February and confirmed in a follow-up proposal in spring 2023. However, the pulsar was also found by the CHIME/FRB system³⁶ and its timing solution has since been reported in Dong et al. (2023). We include it on the survey website (located at https://gbncc.github.io/GBT820_results/gbt820.html) as a codiscovery. Pulsar parameters for all new sources are presented in Table 4 (including those measured from timing campaigns where appropriate), and will be discussed in more detail below. We also include information about the follow-up conducted for relevant sources in Table 5. Additionally, discovery parameters for all new sources are listed on the survey’s website.

5.1. PSR J2057+4701

Initially noted as a faint candidate, PSR J2057+4701 was included in a follow-up proposal aimed at confirming survey candidates in early 2023 (project code AGBT23A-332). However, between acceptance of the proposal and the beginning of observations, it was included in a CHIME/Pulsar publication (Dong et al. 2023). After closer inspection, we found that the source is notably brighter in a second beam that is $\sim 0.3^\circ$ away from the first, but this second beam had failed in

³⁵ <http://zmtt.bao.ac.cn/GPPS/GPPSnewPSR.html>

³⁶ Listed on <https://www.chime-frb.ca/galactic>

Table 4
Measured Position and Spin Parameters and Related Derived Parameters for GBT820 Pulsar Discoveries

Parameter Name	J2016+3820	J2016+4231	J2019+3810	J2035+3538	J2035+3655	J2041+4551
Measured Quantities						
R.A. [deg]	303.9(2)	304.2(2)	304.9(2)	308.9(2)	308.7500006(3)	310.25000(3)
Decl. [deg]	38.3(2)	42.5(2)	38.2(2)	35.6(2)	36.931172(4)	45.8496(3)
DM [pc cm ⁻³]	198.4(10)	222(5)	495(4)	219(2)	136.790(9)	310.0(3)
Spin Frequency [Hz]	4.329043438(98)	0.804014(5)	1.903892(7)	2.083420(4)	40.70837860639(7)	0.8622090188(3)
Spin Frequency Derivative [Hz s ⁻¹]	-2.0557(9) × 10 ⁻¹⁵	-1.5704(5) × 10 ⁻¹⁴
Period Measurement Epoch [MJD]	57524	57763	57523	57499	59328	59360
Derived Quantities						
Spin Period [s]	0.230997913(5)	1.24376(7)	0.52524(2)	0.479985(15)	0.02456496756280(4)	1.1598115749(4)
Spin Period Derivative [s s ⁻¹]	1.2405(6) × 10 ⁻¹⁸	2.1125(7) × 10 ⁻¹⁴
Galactic Longitude [deg]	76.0(5)	79.5(5)	76.2(5)	76.0(5)	76.9518573(9)	84.76111(14)
Galactic Latitude [deg]	1.6(4)	4.0(5)	1.1(5)	-3.0(5)	-2.15755730(3)	2.312631(4)
Magnetic Flux Density [Gauss]	5.59 × 10 ⁹	5.01 × 10 ¹²
Spin-down Energy [ergs s ⁻¹]	3.31 × 10 ³³	5.35 × 10 ³²
Characteristic Age [Myr]	3.13 × 10 ²	8.67 × 10 ⁻¹
DM Distance [kpc]	6.0/6.7	9.0/9.3	19./50	9.5/8.2	5.4/5.5	9.0013.5

Note. Uncertainties in parentheses are 1σ on the last digit. The range of precision for measured values is due to varied baselines: J2035+3655's binary follow-up included many observations over several years, and so a full timing solution was determined; J2041+4551 was observed at 1400 and 820 MHz with the GBT and also at CHIME (600 MHz); and J2016+3820 was confirmed via detection in several survey beams, but was not followed up otherwise. DM distances are calculated using YMW+16/NE2001; we assume a braking index of three to calculate age, and moment of inertia $I = 10^{45}$ g cm² to calculate the surface magnetic flux density.

Table 5
Follow-up Observation Information for GBT820 Discoveries

Observatory	MJD	$\nu, \Delta\nu$ (MHz)	Duration (min)	N_{TOAs}
J2035+3655				
GBT	59328	820, 200	16	10
	59364	820, 200	10	6
	59367	820, 200	10	6
	59368	820, 200	7	6
	59400	1500, 400	20	6
	59611	1500, 400	200	60
	59617	1500, 400	215	60
	59622	1500, 400	224	60
J2041+4551				
GBT	59364	820, 200	20	48
	59400	1500, 400	18	60
CHIME	59270–59385	600, 400	10/day ^a	145

Note.

^a Due to scheduling complexities, CHIME observations were not strictly daily, but averaged about five scans per week (each lasting for 10 minutes).

initial processing. We then searched archival GBNCC data and noted a highly scattered pulse there as well, which we discuss in Section 6.1.

5.2. PSR J2016+3820

PSR J2016+3820 was initially identified in two neighboring survey beams and later found in two other beams. This pulsar is notable for its similarities to PSR J2013+3845 (Hobbs et al. 2004) in spin period ($\leq 1\%$ difference) and position ($\approx 50'$ offset). However, the DM differs by ≈ 39 pc cm⁻³. While the discovery parameters for J2016+3820 are limited in precision, previous timing of J2013+3845 in Hobbs et al. (2004) indicate that these parameter differences are very significant ($>100\sigma$ in

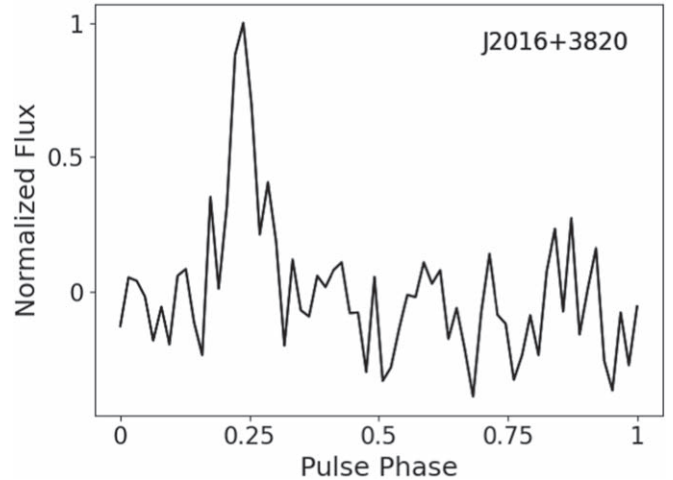


Figure 4. Pulse profile for PSR J2016+3820. The flux density information for this source is reported in Table 2; the discovery parameters are included in Table 4.

period and DM). As a definitive check, the known timing-derived model for PSR J2013+3845 was used to fold the observation in which PSR J2016+3820 was discovered, and the former was not detected.

Using the PRESTO suite, the five detections of this pulsar were manually cleaned of RFI and used to produce arrival times for the pulses (hereafter called times of arrival (TOAs)). These TOAs were then analyzed using PINT (Luo et al. 2021). The four detections in the survey data span less than a week, but the confirmation scan was conducted over 5 yr later. Given this sparse data set, and the many covariant model components that impact the predicted pulse phase over such a gap, we can only place weak upper limits on the timing parameters. We report the spin period from timing in Table 4, but the position reported there is uncertain to within a survey beam ($\approx 15'$), and the period derivative is not constrained. The profile for this source is shown in Figure 4.

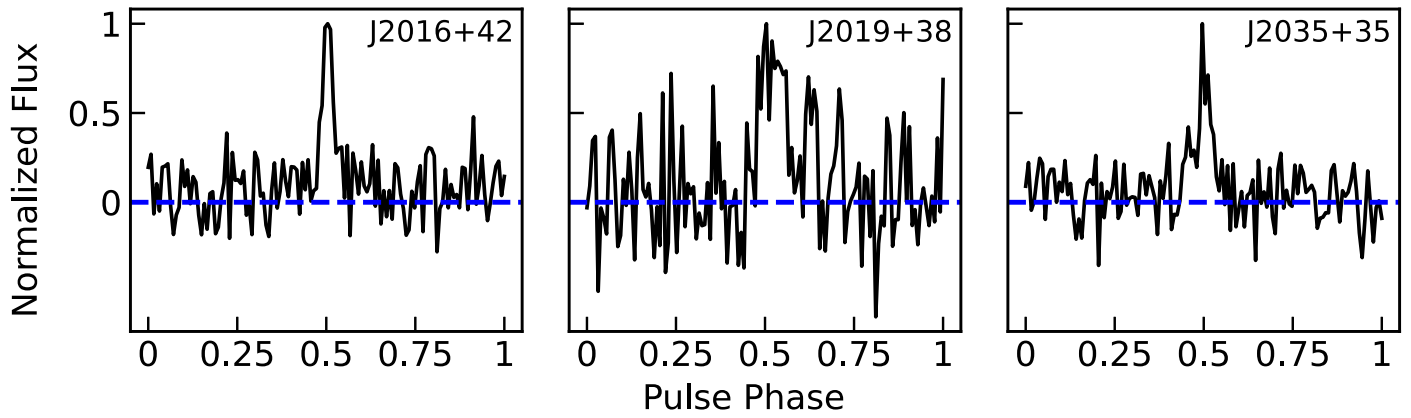


Figure 5. Pulse profiles for three pulsars: PSRs J2016+4231, J2019+3810, and J2035+3538, discovered in the PEASOUP processing of the GBT820 survey. Each profile is generated from its discovery observation using 128 phase bins and has been rotated such that the signal peaks at 0.5 phase.

5.3. PSRs J2016+4231, J2019+3810, and J2035+3538

After the PEASOUP processing (including candidate sorting and folding) described in Section 3.2, we inspected about 10,000 candidates and found five which resembled the properties of a pulsar. Three of them were initially confirmed in the nearest beams of the survey itself. PSR J2016+4231 was redetected in two other beams with similar S/N, while two other pulsars (J2035+3538 and J2019+3810) were each found in a single neighboring beam. Their spin periods place them among canonical pulsars (see Table 4). Of more interest is the DM of PSR J2019+3810, which is the largest of the discoveries (495 pc cm^{-3}). This is above the maximum predicted along this line of sight by NE2001 (393 pc cm^{-3}) and just shy of that predicted by YMW+16 (498 pc cm^{-3}), suggesting that NE2001 greatly underpredicts the DM in this region.

Due to the timing of these discoveries, only minimal analysis is conducted here, with a more complete picture in an upcoming work (R. Sengar et al., 2024, in preparation). Nonetheless, we include the discovery parameters in Table 4 and measured pulse widths and flux densities at 820 MHz in Table 2. We also include the profiles for these three pulsars in Figure 5.

5.4. PSR J2041+4551

PSR J2041+4551 was the first discovery in the survey, and is a slower pulsar (spin period of 1.16 s). It was detected in four survey beams, and follow-up was conducted using CHIME over several days (for an overview of the CHIME system, see CHIME/Pulsar Collaboration et al 2021). While the pulse was not visible in a single day’s observation with CHIME, summing together six 20 minute observations from multiple days produced a detection of a highly scattered pulse. We continued to observe with CHIME for 74 days and split the 400 MHz of the bandwidth into two subbands for DM refinement through timing. It was also included in a Director’s Discretionary Time (DDT) proposal for the GBT (GBT21A-405, PI: A. McEwen) along with J2035+3655, which included a total of 2.5 hr of observations using the 820 MHz receiver. Most of this time was used for J2035+3655, but ~ 20 minutes were used to drift over J2041+4551’s position in both R.A. and decl. (on-the-fly mapping, as in Swiggum & Gentile 2018) and localized the pulsar to well within a 820 MHz beam at the GBT. The final observations

were conducted using the 1400 MHz *L*-band receiver on the GBT, and consisted of a single 17 minute scan. Using the detections in the survey, the CHIME data, and the GBT observations, pulse TOAs were generated using tools within PRESTO and timed using PINT. The resulting parameters of the fit are included in Table 4, and the residuals are shown in Figure 6.

5.5. PSR J2035+3655

PSR J2035+3655 was discovered in two adjacent survey beams with an observed spin period of 24 ms. This period puts J2035+3655 in a sparse region of the $P - \dot{P}$ plane containing partially recycled binaries and young, energetic pulsars (see Figure 3). These two subpopulations are distinguished by intrinsic \dot{P} , which is not generally detectable in survey scans. For the former scenario, the companion undergoes a supernova before the pulsar has accreted enough material to reach a <10 ms rotation period. The supernova occurs when the companion is a more massive star; therefore, it is a marker for potential double-neutron-star systems (Tauris et al. 2017).

This possibility spurred immediate follow-up observations at CHIME and the DDT proposal described in Section 5.4. Unfortunately, J2035+3655 was not detected with CHIME, so high-cadence observations were not possible. Mapping scans with the GBT were successful, greatly improving the position and providing evidence of a time-varying spin period. A subsequent proposal (GBT22A-053, PI: A. McEwen) for 12 hr of observations at 1400 MHz with the GBT was accepted, and the time was split over three 4 hr observations spanning a week. This cadence allowed us to observe a significant portion of the binary orbit in a single observation and maintain coherence over the week.

With these data, we measured the parameters of the orbit with high significance. These constraints (along with those from the mapping scans) reduced our phase uncertainty enough to connect all of the data, including those in the initial survey beams. The resulting data set contained 227 TOAs spanning >2000 days grouped in 11 epochs. Using PINT and the binary model measured in the high-cadence data, we constrained the rotational model for the pulsar. The rotational parameters are included in Table 4, and the binary model is in Table 6. We also include a measurement of the system’s mass function,

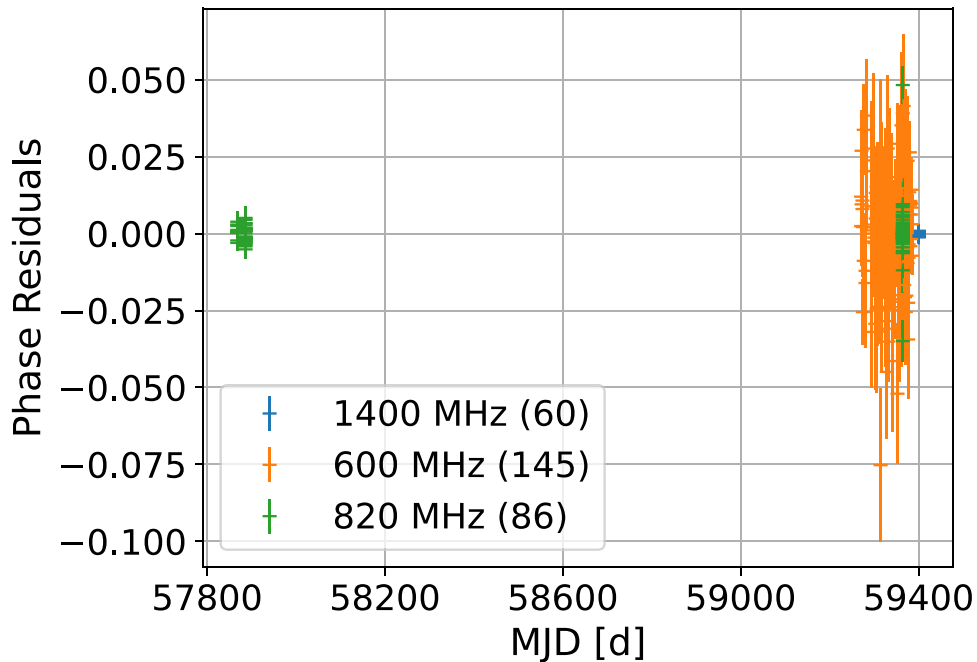


Figure 6. Timing residuals for PSR J2041+4551. Shown as residuals in pulse phase, we include TOAs from three observing setups: green points are the GBT820 survey data, orange are from CHIME (two frequency bands per epoch), and blue are from the 1.4 GHz DDT observations with the GBT.

derived using Equation (8.34) in Lorimer & Kramer (2012)

$$f(M_P, M_C) = \frac{(M_C \sin i)^3}{(M_P + M_C)^2} = \frac{4\pi^2 x^3}{T_\odot P_B^2}, \quad (3)$$

where M_C and M_P are the companion and pulsar masses, respectively, i is the orbital inclination, $T_\odot = (GM_\odot c^{-3}) = 4.925490947 \mu\text{s}$ is a constant to express the masses in solar units, $x = A_1/c$ is the projected semimajor axis in units of seconds, and P_B is the orbital period.

With the phase-connected solution covering superior conjunction in hand, we attempted to measure the Shapiro delay (SD; for the original derivation, see Shapiro 1966; for its measurement in the context of pulsar timing, see Kramer et al. 2006). To do this, we conducted a grid search over the orbital inclination and companion mass and calculated the resulting rms of the residuals. We limited the search to solutions in which the pulsar mass $M_P > 1 M_\odot$ and the companion mass $M_C < 2 M_\odot$. This technique resulted in a marginal ($\simeq 2\sigma$) detection of M_C and the sine of the orbital inclination, $\sin i$. The grid and 1D projections of the χ^2 for points close to the best fit are shown in Figure 7, where we have zoomed in on $\sin i > 0.97$ to highlight the region of most support. We also include timing residuals in Figure 8 with the putative SD signal shown.

6. Analysis and Discussion

6.1. Pulse Scattering

In a simplified Galactic model, GBT820 peers through three spiral arms: the local/Orion arm, the Perseus arm, and a distant third arm. Since stars primarily form in the Galactic arms, we expect that pulsars may be clustered in DM around the mean values for each arm. In reality, the distribution of material in this direction is still under debate, as many recent Gaia studies have provided new measurements of the distribution of dust in Cygnus (Orellana et al. 2021; Vergely et al. 2022).

Table 6
Binary Parameters for PSR J2035+3655

Parameter	Value	Unit
Measured Quantities		
Orbital Period, P_B	0.19272782022(18)	days
Projected Semimajor Axis, A_1	2.180121(3)	lt-s
Epoch of Ascending Node, T_{ASC}	59611.66149639(5)	MJD
Laplace-Lagrange parameter 1, ϵ_1	2(3)	10^{-6}
Laplace-Lagrange parameter 2, ϵ_2	21(3)	10^{-6}
Companion Mass, M_C	0.9(5)	M_\odot
Derived Quantities		
Orbital Eccentricity, e	21(4)	10^{-6}
Inclination, i	$88.2^{+0.1}_{-50.6}$	deg
Pulsar Mass, M_P	0.7(7)	M_\odot
Mass Function, $f(M_P, M_C)$	0.2995268(12)	M_\odot

Note. Uncertainties in parentheses are 1σ on the last digit.

Nevertheless, detections of pulsars sample the ISM along lines of sight through these arms, and examining the effects of scattering on their profiles provides another measure of the content of this material. To measure the scattering timescale for a given profile, following Krishnakumar et al. (2017) we assume that the broadened pulse is

$$P(t) = P_i(t) * s(t) * D(t) * I(t). \quad (4)$$

In this expression, $*$ denotes convolution, p_i is the intrinsic (unscattered) pulse, $s(t)$ describes the impulse response from scattering, $D(t)$ is a step function with width specified by the predicted DM smearing due to finite channelization, and $I(t)$ contains additional temporal smearing due to finite phase binning. Here, the frequency channel/phase bin widths are small enough that smearing due to $D(t)$ and $I(t)$ can be neglected. The impulse response for exponential scattering is

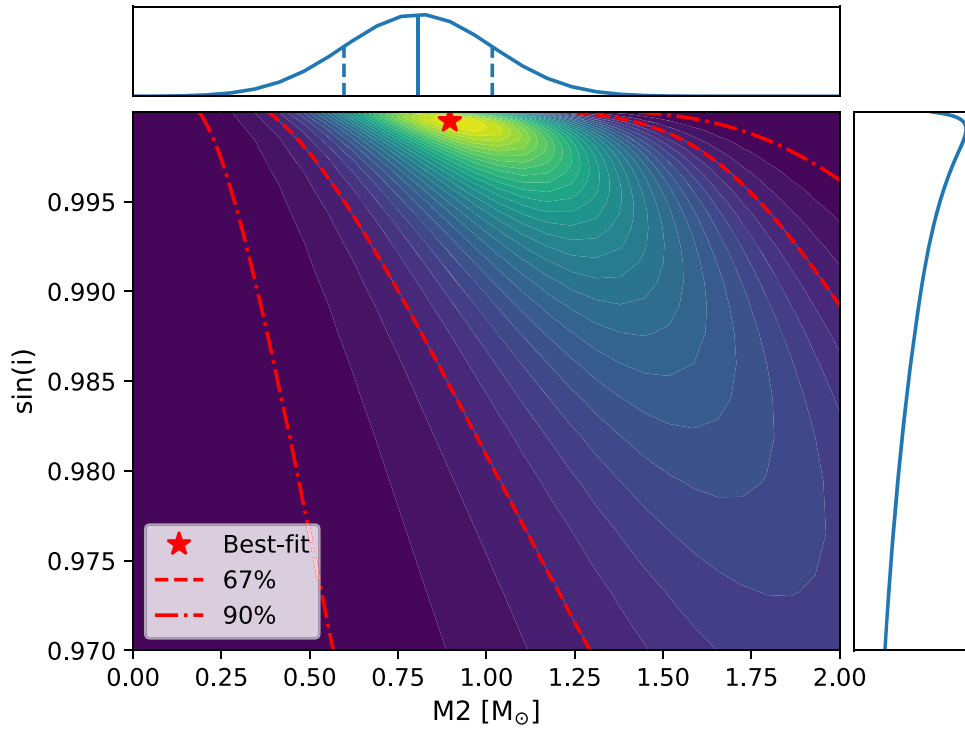


Figure 7. Results of the $M_C - \sin i$ grid for PSR J2035+3655. We show the map of grid values with contours of constant probability density function, and include a marker for the best-fit point and contours for the 67% and 90% confidence levels. This measurement equates to an $\simeq 2\sigma$ detection of the SD parameters. Also plotted are the marginal probability density functions of both measured parameters, along with the mean (solid) and 1σ (dashed) lines for M_C . The grid used for $\sin i$ extended below 0.97, but only this region is included as it has the most support.

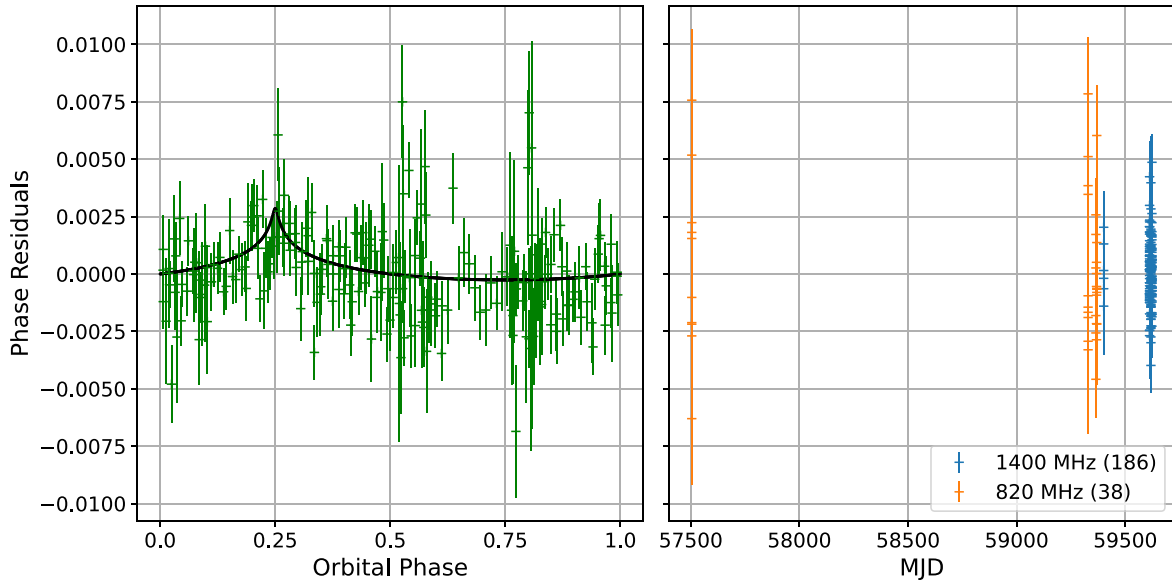


Figure 8. Timing residuals for PSR J2035+3655. In the left panel, we plot the phase residuals against orbital phase, and plot the measured SD signal in black. Note that the model used to produce these residuals does not include the SD parameters. On the right, we plot all residuals colored by observing frequency. Unlike the left panel, these residuals do include the SD model.

modeled as

$$s(t) = \exp(-t/\tau_{sc})U(t - t_p), \quad (5)$$

where τ_{sc} is the scattering timescale and $U(t)$ is a step function that defines the first bin of the exponential kernel, located at t_p . To enrich our results, we supplement the profiles as measured in the GBT820 survey with additional profiles at different frequencies. For seven of these sources, listed in Table 7, additional profiles come from detections in the GBNCC survey

at 350 MHz. Pulsars J2035+3655 and J2041+4551, discoveries from the GBT820 survey, were not detected in GBNCC. However, other follow-up for these sources was conducted at 1400 MHz (with the GBT), and J2041+4551 was observed at 600 MHz (with CHIME). For these sources, we use the 1400 MHz profile as the intrinsic profile. We also use J2041+4551’s CHIME profile as the “scattered” profile. For all other pulsars, we use the 820 MHz profile as the intrinsic profile. After subtracting the baselines, we normalize the profiles from

Table 7
Scattering Timescales (Scaled to 350 MHz) from Multifrequency Profile Comparison

PSR	τ_{sc} (ms)	DM (pc cm^{-3})
J2002+4050	22.0 (4)	131.5
J2006+4058	70 (20)	259.5
J2013+3845	16.3 (6)	238.2
J2027+4557	30 (2)	229.6
J2029+3744	13.9 (9)	190.7
J2035+3655	1.0 (2)	136.7
J2037+3621	10.8 (6)	93.6
J2041+4551	186 (4)	310.0
J2057+4701	27 (7)	219.0

Note. The values in parentheses are the uncertainties on the last digit that have been scaled such that the reduced χ^2 values for the fits to the profiles are 1.

both data sets by their sums and convolve the higher-frequency profile with $s(t)$. We then subtract the broadened pulse from the lower-frequency profile and calculate the χ^2 of the residuals. With this scheme, we performed a grid search over tp and τ_{sc} to minimize the χ^2 . These fits, along with their matching low- and high-frequency profiles, are shown in Figure 9, with the inferred scattering timescales in Table 7.

To put our scattering measurements in context, we plot them with several comparisons in Figure 10. Measurements for all nine sources are included with the predictions from NE2001 and YMW+16. Scatter about the Bhat et al. (2004) best-fit line (orange dashed line) is expected, as is evident from other catalog measurements of τ_{sc} (gray crosses in Figure 10), though it is apparent that the NE2001 predictions are systematically low. There may be a plateau in our measured τ_{sc} for sources below 300 pc cm^{-3} , which matches Bhat et al. (2004) and Krishnakumar et al. (2015) more closely towards higher DMs.

6.2. Cygnus Pulsar Population

At the time of the survey proposal (2016), estimates for the survey’s yield predicted as many as 65 new pulsars in the Cygnus region, including five new millisecond pulsars (MSPs). Given that about two-thirds of the survey was observed, we might have expected close to 40 new pulsars in this region. Our discovery of only six pulsars, one of which could be classified as an MSP, suggests a relative dearth of sources detectable at 820 MHz using the GBT. Subsequent surveys utilizing FAST have uncovered several sources in this region that lie below this survey’s predicted sensitivity limit, which we illustrate in Figure 11. To quantify the sensitivity of the survey, we plot the predicted flux density at 820 MHz as calculated by Equation (2). We utilize the minimum search S/N of a detection in the survey (six) to scale these curves, and account for pulse smearing due to scattering by modeling the width of a pulse as

$$W_{sm} = \sqrt{W_{int}^2 + \tau_{sc}^2}. \quad (6)$$

We assume the intrinsic pulse width (W_{int}) to be 6% of the pulse period (Johnston & Karastergiou 2019; McEwen et al. 2020) and calculate the predicted scattering τ_{sc} using the expression in Bhat et al. (2004). This results in the asymptotic behavior seen in the flux density curves toward short periods since pulses with widths that are greater than or equal to the

pulse period will not be detectable. With these parameters, we find the 3σ minimum flux density measurable (with a known pulsar solution) in the survey to be 0.24 mJy. For the search pipeline, which uses an S/N of six as the cutoff, the 3σ minimum flux density detectable is 0.35 mJy.

Given the discrepancy between the predictions and survey yield, we examined the differences between the simulated discoveries and the pulsars known to exist in the region, as well as those discovered by GBT820. To do so, we utilized `PsRPopPy`³⁷ (Bates et al. 2014) to generate pulsars in this region and attempted to “detect” them using the survey parameters for GBT820. This will depend on the pulsar’s intrinsic brightness as well as its period–DM combination, as shown in Figure 11. To produce simulated populations, `PsRPopPy` draws from user-specified distributions of pulsar spin and position parameters. The simulated position is mapped onto Galactic models of the ISM, and the expected DM is calculated. With these parameters, the code then assesses the detectability of the pulsar in a collection of user-specified pulsar surveys. These surveys are chosen to cover a wide range of observing frequencies and sky positions to avoid biases from individual survey setups. The simulations here utilized the total number of pulsar/MSP detections from the following surveys, where we define an MSP as having a period ≤ 30 ms: GBNCC (670/70; McEwen et al. 2020), AODrift (75/33; Martinez et al. 2019), PALFA (207/46; Parent et al. 2022), LOTAAS (300/11; Coenen et al. 2014; Sanidas et al. 2019), PMPS (916/28; Sengar et al. 2023), PKS70 (298/17; Lyne et al. 1998), and SMART (180/14; Bhat et al. 2023). We supplied the total number of known pulsar detections from all of these surveys, N_{tot} , and `PsRPopPy` generates pulsars until N_{tot} is detected. At this point, the simulated population of pulsars is “observed” by a model for the GBT820 survey, and the number/characteristics of the simulated sources that are detected are compared to the actual sample of observed pulsars. Details of the parameters used for the `PsRPopPy` simulations are given in Table 8.

By determining the median values of pulsar parameters as a function of the number of populations included, we found that all parameters stabilize with ≥ 100 independent populations. For the following analysis, we included 300 such populations. Given the input survey information listed above, we find that the predictions for the number of MSPs detected match the actual survey yield of two detections. However, canonical pulsar detections are underpredicted, with a median of 11 simulated detections compared to 23 detections.

Beyond the number of sources, we examined the distribution of spin periods and DMs for the simulated detections against those of the real pulsars in the survey region. We find some notable discrepancies, particularly in DM, where there are many simulated pulsars with $DM \leq 100 \text{ pc cm}^{-3}$. In Figure 12, we include histograms of both period and DM for the simulated population of canonical pulsars with the actual pulsars in this survey region (both detected and nondetected sources are shown). We calculate the median value of both parameters and plot them with their 1σ regions shaded.

The median spin period for the simulated canonical pulsars (spin period ≥ 30 ms, Figure 12) is slightly higher than the median of either the detected or nondetected populations, though the more clearly discrepant parameter is pulsar DM. Simulations produced nearly half of all detections with DMs

³⁷ <https://github.com/samb8s/PsRPopPy>

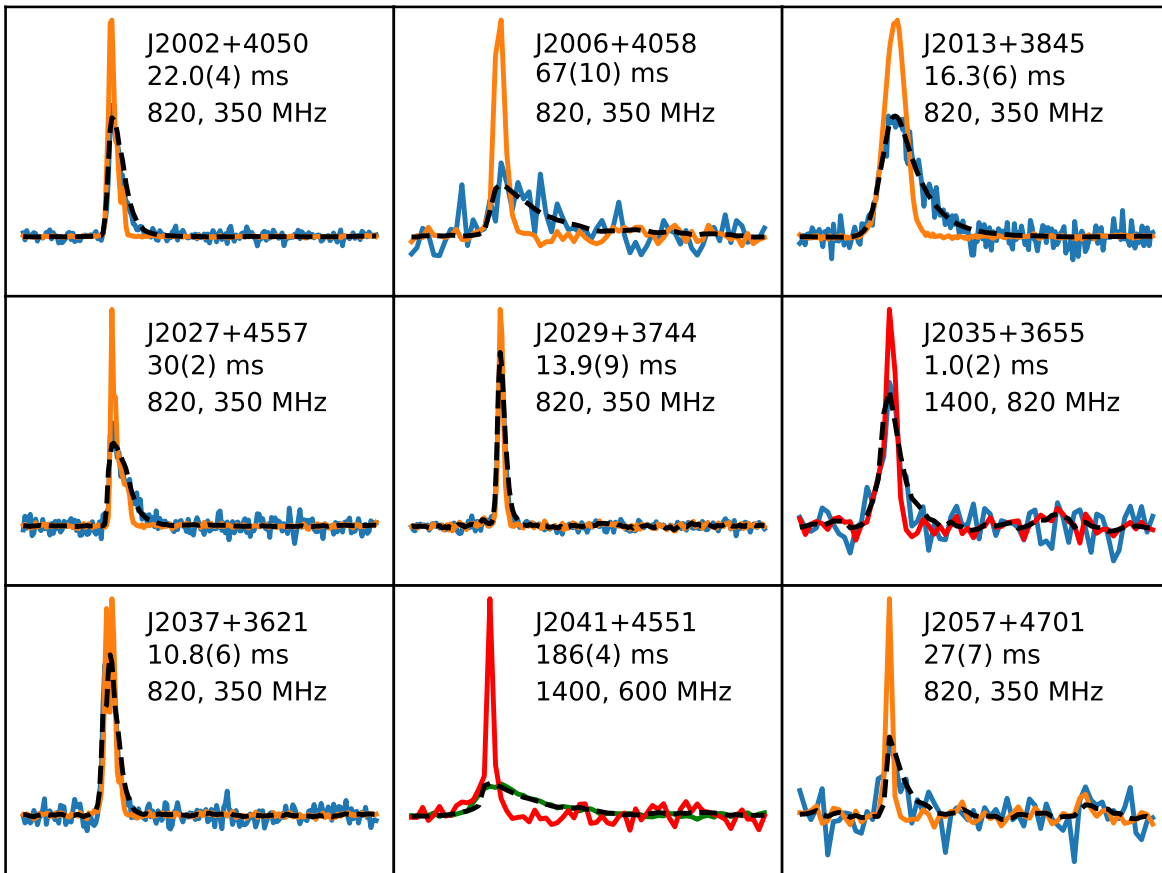


Figure 9. Scattered profiles. Shown in solid lines are the profiles used to measure scattering. Colors correspond to different observing frequencies, where blue is 350 MHz, green is 600 MHz, orange is 820 MHz, and red is 1400 MHz. We include the scattering timescale measurement and the observing frequencies for the reference and scattered profiles in each panel. For all pulsars except the survey discoveries (J2035+3655 and J2041+4551), the GBT820 detection is the reference profile, and the GBNCC detection is the scattered counterpart. For J2035+3655, the 1400 MHz observation serves as the reference profile and the GBT820 detection is scattered. For J2041+4551, the 1400 MHz observation is the reference, and the CHIME data are the scattered profile. With dashed black lines, we show the convolution of the reference pulse with an exponential scattering kernel. All profiles include a full rotation of the pulsar.

below that of the nearest known pulsar in the survey (J2108+4516, $DM = 84.0 \text{ pc cm}^{-3}$). As the GBT820 survey should be quite sensitive to such DMs from a scattering perspective (for $DM \leq 100 \text{ pc cm}^{-3}$, predicted $\tau_{sc} \leq 21 \mu\text{s}$, likely much less than 10% of the width of a pulse), and scintillation would only result in significant modulation to sources $\lesssim 10 \text{ pc cm}^{-3}$, this may imply an overestimate of low-DM sources in population models. Such an overestimate could be explained by an overdense region of the Galaxy (like the Cygnus region) in which a given line of sight will accumulate dispersive delays quickly over a relatively short distance. This would imply (1) the maximum DM in the survey region is larger than what is predicted; (2) the DMs of pulsars in the Cygnus region with independent distance measurements will be higher on average than what is predicted using standard distance-to-DM models (YMW+16 and NE2001); and (3) there are fewer than average detectable radio MSPs.

The first of the above consequences may be supported by the growing collection of sources detected by the FAST-GPPS survey (Han et al. 2021) with excessive DMs. The maximum DM predicted in the survey region is $\approx 500 \text{ pc cm}^{-3}$ for both NE2001 and YMW+16; this threshold is surpassed by six of the sources listed (including J2051+4434g, detected in GBT820). The second point can be tested using catalog measurements of distance. Three of the pulsars in the survey with published DMs have independent distance measurements:

J2022+3842 (10 kpc, SNR association; Arzoumanian et al. 2011), J2021+3651 (1.8 kpc, red star association; Kirichenko et al. 2015), and J2032+4127 (1.33 kpc, spectroscopic observations of eclipsing binaries; Kiminki et al. 2015). All of these distance measurements are well below what is predicted by their DMs (13.2, 10.5, and 4.6 kpc, respectively, per YMW+16). In fact, such an overdensity in DM is mentioned by Arzoumanian et al. (2011) to explain this discrepancy for J2022+3842, and Table 5 of Cordes & Lazio (2002) includes measurements of so-called “clump parameters” used to account for excess scattering along many Cygnus lines of sight. Also notable in that sample is the difference in distances for J2021+3651 (discussed in Hessels et al. 2004) and J2032+4127 (0.5 kpc) compared to the difference in their DMs (253 pc cm^{-3}). Gaia observations have been used to find clusters of dusty OB regions at distances $\approx 1.4 \text{ kpc}$ (Orellana et al. 2021; Quintana & Wright 2022), which may support a complex line-of-sight dependence for DM.

For MSPs, the simulated populations reflect the opposite situation: the median detected periods of these sources are discrepant (though less so), while the DMs are in more agreement. However, with so few MSPs in this direction (J2035+3655 and J2053+4650 are the only known radio-bright MSPs), making meaningful statements about their characteristics is difficult. This relative dearth of MSPs supports the argument above: if DMs are larger than average

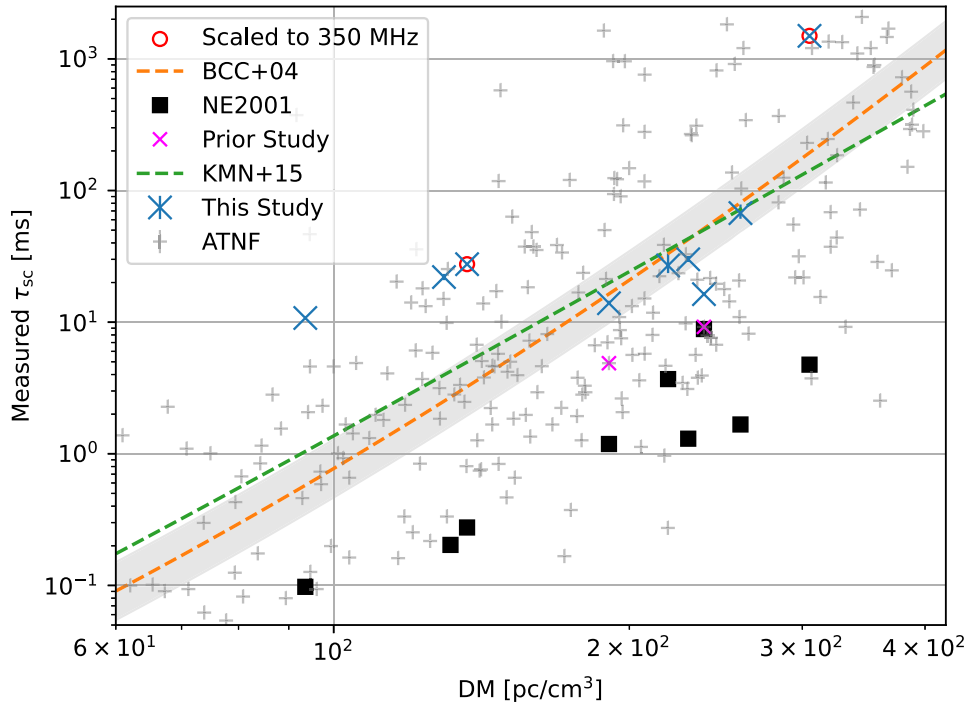


Figure 10. Scattering timescales of pulsars measured in the GBT820 data, along with archival data, scaled to 350 MHz. Plotted with blue Xs are the measurements made in this study, listed in Table 7; those that are highlighted with red circles indicate pulsars for which we measure τ_{sc} at a frequency other than 350 MHz and scale using a power law with index $\alpha = 3.86$ from Bhat et al. (2004). We include the relation published in that work in orange with the 3σ uncertainty region on α in gray. A more recent review (Krishnakumar et al. 2015) published a similar relation, which we plot using a green dashed line. For each pulsar, we calculate the scattering timescales as predicted by NE2001 (Cordes & Lazio 2002) and plot them using black squares. We also include all ATNF measurements of τ_{sc} for pulsars in this range of DMs, shown in gray. We have scaled these from 1 GHz to 350 MHz using $\alpha = 3.86$, though there may be additional scatter from different observing setups. Two sources included in this study (J2029+3744 and J2013+3845, with DMs of 190.6 and 238.2 pc cm^{-3} , respectively) have values of τ_{sc} published in ATNF; these are plotted as magenta Xs.

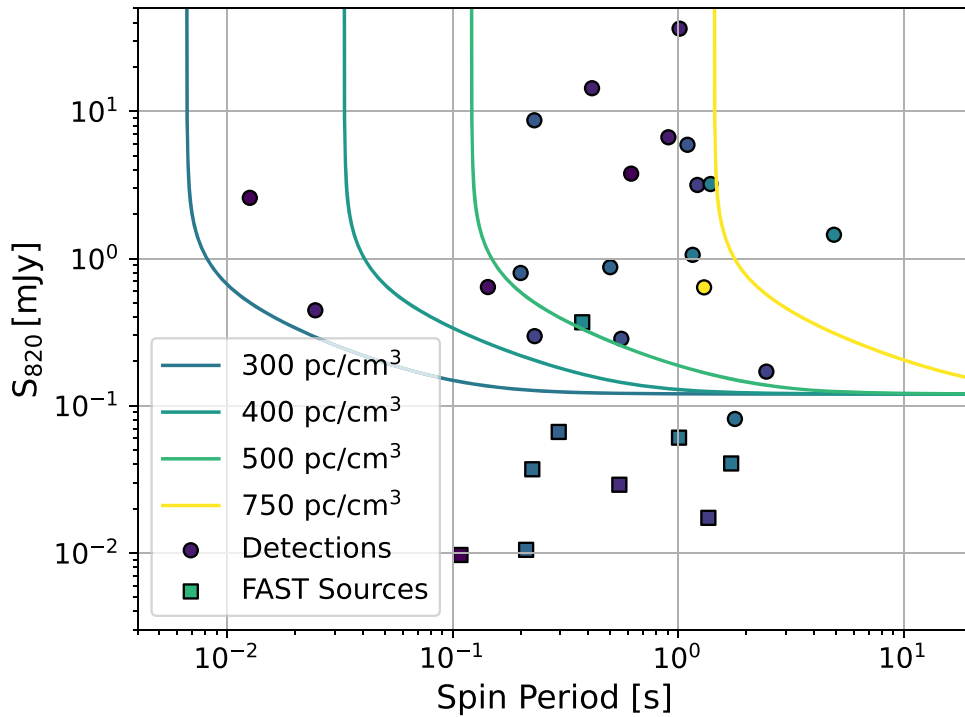


Figure 11. GBT820 sensitivity curve showing the pulsars detected in GBT820 using filled circles and the FAST discoveries that were not detected in the survey with filled squares. All sources are colored by their DM. Curves show lines of constant DM; asymptotes at short periods are the result of modeled pulse smearing, which spans beyond a single rotation for fast, distant sources. The detection that lies below the sensitivity curve is the FAST-detected pulsar J2026+3656g (Han et al. 2021), which we detected only after using the previously determined rotation model with an S/N of four, below the search threshold of six. Also, the single FAST nondetection that lies just above the sensitivity curve is J2052+4421g (DM = 547 pc cm^{-3}), which shows visible scattering at 1.25 GHz (profile available at <http://zmtt.bao.ac.cn/GPPS/GPPSnewPSR.html> and published in Han et al. 2021).

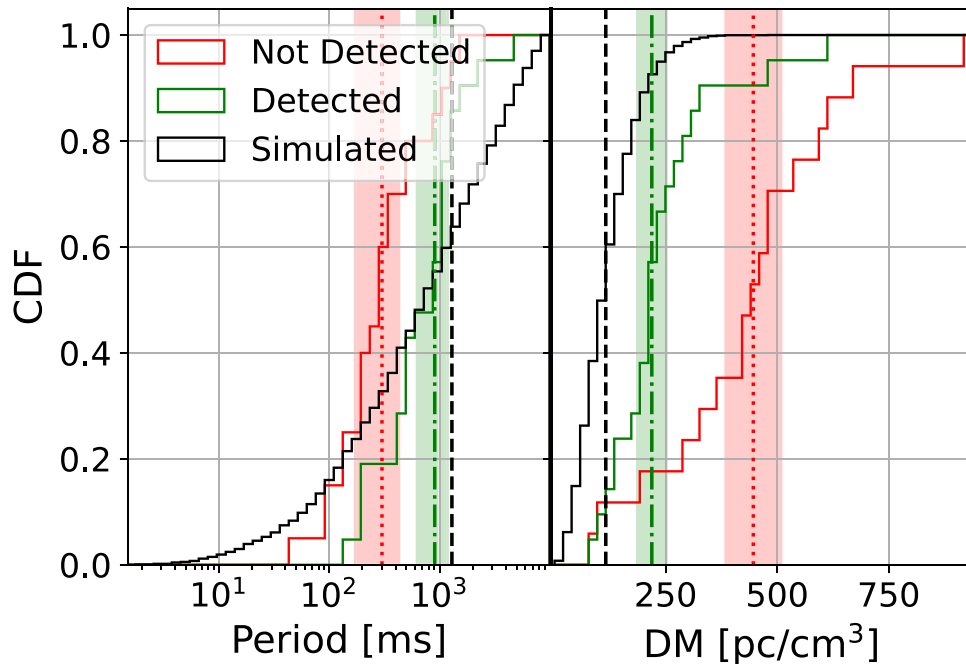


Figure 12. Comparison of known canonical pulsars to simulations. We plot the cumulative distributions of spin period (left) and DM (right) for three subpopulations: the simulated sources (black), the known pulsars that were detected in GBT820 (green), and those that were not detected (red). For each, we plot a vertical line (dashed, dot-dashed, or dotted for each respective subpopulation) at the median value and shade the 1σ region. We excluded some simulated detections with periods too large ($P \geq T_{\text{obs}}/2$) to be detected in GBT820. All sources have spin periods greater than 30 ms. The period distributions are fairly well matched, but the simulated pulsars have significantly smaller DMs on average.

Table 8
Overview of the Relevant `PsRPopPy` Parameters

Parameter Name	Value/Range	Description
All Simulations		
<code>surveys</code>	“GBNCC,” “AODRIFT,” “LOFAR,” “PALFA3,” “PMSURV,” “PKS70,” and “SMART”	Surveys used to produce the simulated populations (see note)
Pulsars		
<code>ngen</code>	670, 75, 300, 207, 916, 298, and 180	Known pulsar detections in the above surveys
<code>pDistType</code>	“lnorm”	lognormal
<code>pDistPars</code>	[3, 1]	μ , σ of the period distribution [log(ms)]
MSPs		
<code>ngen</code>	70, 33, 11, 46, 28, 17, and 14	MSP detections in the above surveys
<code>pDistType</code>	“lorimer12”	Lorimer et al. (2015)
<code>pDistPars</code>	[1.5, 0.58]	μ , σ of the period distribution [log(ms)]

Note. Parameters omitted from this list were left to the default values as shown in `PsRPopPy` documentation (<https://github.com/samb8s/PsRPopPy>). Detection counts for the surveys come from the following: GBNCC (McEwen et al. 2020), AODrft (Martinez et al. 2019), PALFA (Parent et al. 2022), LOTAAS (Coenen et al. 2014; Sanidas et al. 2019), PMPS (Sengar et al. 2023), PKS70 (Lyne et al. 1998), and SMART (Bhat et al. 2023).

along the line of sight, scattering will mask even the brightest MSPs. So while there may be many more MSPs in the region, radio detection will be difficult, regardless of telescope sensitivity. However, higher-frequency observations may be more fruitful, as they sidestep the issue of dispersive smearing. This is reflected in the number of gamma-ray and X-ray sources that are known in Cygnus.

7. Conclusions

The GBT820 survey of the Cygnus region has yielded six previously undiscovered pulsars, including five canonical pulsars and an MSP in a close, near-circular binary, likely

with a white dwarf companion (J2035+3655). We have measured spin and position parameters for all of these pulsars, though with widely varying precision due to different follow-up strategies. We also utilized published parameters/profiles for the known sources in the region to measure the flux density for each and estimate the survey’s sensitivity. Finally, we measured scattering parameters for nine pulsars.

While these discoveries fall short of the initial predictions for this region, we find that the future may not be so dim. If it is true that this region has an overdensity of free electrons that reduces the efficiency of radio searches, then nondetections may only indicate that the region should be observed at higher

frequencies, and may still harbor exotic sources. FAST surveys in this region have continued to fill out the true DM range of its pulsars; it is likely that most/all radio pulsars in Cygnus will be found in these surveys. Searches using X-ray and gamma-ray observatories will not only see clearly though radio-opaque regions, they will find the young, energetic magnetars and gamma-ray repeaters born in these regions.

Acknowledgments

This work was supported by the NANOGrav Physics Frontiers Center, which is supported by the National Science Foundation award 1430284. The Green Bank Observatory is a facility of the National Science Foundation (NSF) operated under cooperative agreement by Associated Universities, Inc. CHIME is funded by grants from the Canada Foundation for Innovation (CFI) 2012 Leading Edge Fund (Project 31170), the CFI 2015 Innovation Fund (Project 33213), and by contributions from the provinces of British Columbia, Quebec, and Ontario. This research was enabled in part by support provided by Calcul Québec (<https://www.calculquebec.ca/en/>) and the Digital Research Alliance of Canada (alliancecan.ca). Portions of this work performed at NRL were supported by ONR 6.1 funding.

Facilities: The Green Bank Observatory (formerly NRAO) 100m Robert C. Byrd Green Bank Telescope and The Canada Foundation for Innovation Canadian Hydrogen Intensity Mapping Experiment (CHIME).

Software: Astropy (Astropy Collaboration et al. 2013, 2018, 2022), `dspsr` (van Straten & Bailes 2011), PRESTO (Ransom 2001), `SciPy` (Virtanen et al. 2020), `NumPy` (Harris et al. 2020), PSRCHIVE (Hotan et al. 2004), PINT (Luo et al. 2021), `PsrPopPy` (Bates et al. 2015), `PyGEDM` (Price et al. 2021), and `PyGDSM` (Price 2016).

ORCID iDs

A. E. McEwen  <https://orcid.org/0000-0001-5481-7559>
 R. S. Lynch  <https://orcid.org/0000-0001-5229-7430>
 D. L. Kaplan  <https://orcid.org/0000-0001-6295-2881>
 C. Bolda  <https://orcid.org/0000-0002-6913-8580>
 R. Sengar  <https://orcid.org/0000-0002-9409-3214>
 E. Fonseca  <https://orcid.org/0000-0001-8384-5049>
 T. Agoudemos  <https://orcid.org/0000-0001-7084-7328>
 S. Chatterjee  <https://orcid.org/0000-0002-2878-1502>
 T. Cohen  <https://orcid.org/0000-0001-7587-5483>
 F. Crawford  <https://orcid.org/0000-0002-2578-0360>
 M. E. DeCesar  <https://orcid.org/0000-0002-2185-1790>
 E. C. Ferrara  <https://orcid.org/0000-0001-7828-7708>
 W. Fiore  <https://orcid.org/0000-0001-5645-5336>
 J. W. T. Hessels  <https://orcid.org/0000-0003-2317-1446>
 V. Kaspi  <https://orcid.org/0000-0001-9345-0307>
 V. Kondratiev  <https://orcid.org/0000-0001-8864-7471>
 L. Levin  <https://orcid.org/0000-0002-2034-2986>
 D. R. Lorimer  <https://orcid.org/0000-0003-1301-966X>
 D. R. Madison  <https://orcid.org/0000-0003-2285-0404>
 M. A. McLaughlin  <https://orcid.org/0000-0001-7697-7422>
 B. W. Meyers  <https://orcid.org/0000-0001-8845-1225>
 E. Parent  <https://orcid.org/0000-0002-0430-6504>
 S. M. Ransom  <https://orcid.org/0000-0001-5799-9714>
 P. S. Ray  <https://orcid.org/0000-0002-5297-5278>
 M. S. Roberts  <https://orcid.org/0000-0002-9396-9720>
 X. Siemens  <https://orcid.org/0000-0002-7778-2990>
 J. K. Swiggum  <https://orcid.org/0000-0002-1075-3837>

I. H. Stairs  <https://orcid.org/0000-0001-9784-8670>
 K. Stovall  <https://orcid.org/0000-0002-7261-594X>
 C. M. Tan  <https://orcid.org/0000-0001-7509-0117>
 J. van Leeuwen  <https://orcid.org/0000-0001-8503-6958>

References

- Abdo, A. A., Ackermann, M., Ajello, M., et al. 2009, *Sci*, 325, 840
 Abdo, A. A., Ackermann, M., Ajello, M., et al. 2009, *ApJ*, 700, 1059
 Agazie, G. Y., Mingyar, M. G., McLaughlin, M. A., et al. 2021, *ApJ*, 922, 35
 Aggarwal, K., Arzoumanian, Z., Baker, P. T., et al. 2019, *ApJ*, 880, 116
 Arzoumanian, Z., Gotthelf, E. V., Ransom, S. M., et al. 2011, *ApJ*, 739, 39
 Arzoumanian, Z., Baker, P. T., Blumer, H., et al. 2020, *ApJL*, 905, L34
 Arzoumanian, Z., Baker, P. T., Blecha, L., et al. 2023, *ApJL*, 951, L28
 Astropy Collaboration, Robitaille, T. P., & Tollerud, E. J. 2013, *A&A*, 558, A33
 Astropy Collaboration, Price-Whelan, A. M., Sipőcz, B. M., et al. 2018, *AJ*, 156, 123
 Astropy Collaboration, Price-Whelan, A. M., Lim, P. L., et al. 2022, *ApJ*, 935, 167
 Babak, S., Petiteau, A., Sesana, A., et al. 2016, *MNRAS*, 455, 1665
 Bates, S. D., Lorimer, D. R., Rane, A., & Swiggum, J. 2014, *MNRAS*, 439, 2893
 Bates, S. D., Lorimer, D. R., Rane, A., & Swiggum, J. 2015 `PsrPopPy`: Pulsar Population Modelling Programs in Python, Astrophysics Source Code Library, `ascl:1501.006`
 Bates, S. D., Lorimer, D. R., & Verbiest, J. P. W. 2013, *MNRAS*, 431, 1352
 Beerer, I. M., Koenig, X. P., Hora, J. L., et al. 2010, *ApJ*, 720, 679
 Berezina, M., Champion, D. J., Freire, P. C. C., et al. 2017, *MNRAS*, 470, 4421
 Berlanas, S. R., Wright, N. J., Herrero, A., Drew, J. E., & Lennon, D. J. 2019, *MNRAS*, 484, 1838
 Beuther, H., Wyrowski, F., Menten, K. M., et al. 2022, *A&A*, 665, A63
 Bhat, N. D. R., Cordes, J. M., Camilo, F., Nice, D. J., & Lorimer, D. R. 2004, *ApJ*, 605, 759
 Bhat, N. D. R., Swainston, N. A., McSweeney, S. J., et al. 2023, *PASA*, 40, e020
 Bracewell, R. N. 2000, *The Fourier Transform and its Applications* (New York: McGraw-Hill), 209
 Braun, R., Bonaldi, A., Bourke, T., Keane, E., & Wagg, J. 2019, `arXiv:1912.12699`
 Broderick, J. W., Russell, T. D., Fender, R. P., et al. 2021, *MNRAS*, 504, 1482
 Cameron, A. D., Champion, D. J., Bailes, M., et al. 2020, *MNRAS*, 493, 1063
 Camilo, F., Kerr, M., Ray, P. S., et al. 2012, *ApJ*, 746, 39
 CHIME/Pulsar Collaboration, Amiri, M., Bandura, K. M., et al. 2021, *ApJS*, 255, 5
 Coenen, T., van Leeuwen, J., Hessels, J. W. T., et al. 2014, *A&A*, 570, A60
 Comerón, F., & Pasquali, A. 2012, *A&A*, 543, A101
 Cordes, J. M., & Lazio, T. J. W. 2002, `arXiv:astro-ph/0207156`
 Cromartie, H. T., Fonseca, E., Ransom, S. M., et al. 2020, *NatAs*, 4, 72
 Davies, J. G., & Large, M. I. 1970, *MNRAS*, 149, 301
 Davies, J. G., Lyne, A. G., & Seiradakis, J. H. 1973, *NPhS*, 244, 84
 Dewey, R. J., Taylor, J. H., Weisberg, J. M., & Stokes, G. H. 1985, *ApJL*, 294, L25
 Dong, F. A., Crowter, K., Meyers, B. W., et al. 2023, *MNRAS*, 524, 5132
 DuPlain, R., Ransom, S., Demorest, P., et al. 2008, *Proc. SPIE*, Vol. 7019, 70191D
 Emig, K. L., White, G. J., Salas, P., et al. 2022, *A&A*, 664, A88
 Gautam, T., Ridolfi, A., Freire, P. C. C., et al. 2022, *A&A*, 664, A54
 Good, D. C., Andersen, B. C., Chawla, P., et al. 2021, *ApJ*, 922, 43
 Hallinan, G., Ravi, V., Weinreb, S., et al. 2019, *BAAS*, 51, 255
 Han, J. L., Wang, C., Wang, P. F., et al. 2021, *RAA*, 21, 107
 Harris, C. R., Millman, K. J., van der Walt, S. J., et al. 2020, *Natur*, 585, 357
 Haslam, C. G. T., Salter, C. J., Stoffel, H., & Wilson, W. E. 1982, *A&AS*, 47, 1
 Hessels, J. W. T., Ransom, S. M., Kaspi, V. M., et al. 2008, in *AIP Conf. Ser.* 983, 40 Years of Pulsars: Millisecond Pulsars, Magnetars and More, ed. C. Bassa et al. (Melville, NY: AIP), 613
 Hessels, J. W. T., Roberts, M. S. E., Ransom, S. M., et al. 2004, *ApJ*, 612, 389
 Hisano, S., Crawford, F., Bonidie, V., et al. 2022, *ApJ*, 928, 161
 Hobbs, G., Lyne, A. G., Kramer, M., Martin, C. E., & Jordan, C. 2004, *MNRAS*, 353, 1311
 Hotan, A. W., van Straten, W., & Manchester, R. N. 2004, *PASA*, 21, 302
 Janssen, G. H., Stappers, B. W., Braun, R., et al. 2009, *A&A*, 498, 223
 Jiang, P., Peng, B., Li, D., & Xu, R. 2019, `arXiv:1903.07240`
 Johnston, H. M., & Kulkarni, S. R. 1991, *ApJ*, 368, 504

- Johnston, S., & Karastergiou, A. 2019, *MNRAS*, **485**, 640
- Kaplan, D. L., 2022 PSS: Pulsar Survey Scraper, Astrophysics Source Code Library, ascl:2210.001
- Karako-Argaman, C., Kaspi, V. M., Lynch, R. S., et al., 2020 RRATrap: Rotating Radio Transient identifier, Astrophysics Source Code Library, ascl:2011.017
- Keith, M. J., Jameson, A., van Straten, W., et al. 2010, *MNRAS*, **409**, 619
- Kellermann, K. I., Pauliny-Toth, I. I. K., & Williams, P. J. S. 1969, *ApJ*, **157**, 1
- Kiminki, D. C., Kobulnicky, H. A., Vargas Álvarez, Á., et al. 2015, *ApJ*, **811**, 85
- Kirichenko, A., Danilenko, A., Shternin, P., et al. 2015, *ApJ*, **802**, 17
- Koch-Miramond, L., Abraham, P., Fuchs, Y., Bonnet-Bidaud, J. M., & Claret, A. 2002, *A&A*, **396**, 877
- Kramer, M., Stairs, I. H., Manchester, R. N., et al. 2006, *Sci*, **314**, 97
- Krishnakumar, M. A., Joshi, B. C., & Manoharan, P. K. 2017, *ApJ*, **846**, 104
- Krishnakumar, M. A., Mitra, D., Naidu, A., Joshi, B. C., & Manoharan, P. K. 2015, *ApJ*, **804**, 23
- Lentati, L., Taylor, S. R., Mingarelli, C. M. F., et al. 2015, *MNRAS*, **453**, 2576
- Lorimer, D. R., & Kramer, M. 2012, *Handbook of Pulsar Astronomy* (Cambridge: Cambridge Univ. Press)
- Lorimer, D. R., Esposito, P., Manchester, R. N., et al. 2015, *MNRAS*, **450**, 2185
- Luo, J., Ransom, S., Demorest, P., et al. 2021, *ApJ*, **911**, 45
- Lynch, R., Armentrout, W. P., Bonsall, A., et al. 2019, *BAAS*, **51**, 151
- Lyne, A. G., Manchester, R. N., Lorimer, D. R., et al. 1998, *MNRAS*, **295**, 743
- Manchester, R. N., Hobbs, G. B., Teoh, A., & Hobbs, M. 2005, *AJ*, **129**, 1993
- Manchester, R. N., Lyne, A. G., Camilo, F., et al. 2001, *MNRAS*, **328**, 17
- Martinez, J. G., Gentile, P., Freire, P. C. C., et al. 2019, *ApJ*, **881**, 166
- McCullough, M., Corcoran, M., Gendreau, K., et al. 2022, *BAAS*, **54**, 110
- McEwen, A. E., Spiewak, R., Swiggum, J. K., et al. 2020, *ApJ*, **892**, 76
- Merryfield, M., Tendulkar, S. P., Shin, K., et al. 2023, *AJ*, **165**, 152
- Morello, V., Barr, E. D., Cooper, S., et al. 2019, *MNRAS*, **483**, 3673
- Orellana, R. B., De Biasi, M. S., & Paíz, L. G. 2021, *MNRAS*, **502**, 6080
- Özel, F., & Freire, P. 2016, *ARA&A*, **54**, 401
- Parent, E., Sewalls, H., Freire, P. C. C., et al. 2022, *ApJ*, **924**, 135
- Piddington, J. H., & Minnett, H. C. 1952, *AuSRA*, **5**, 17
- Pletsch, H. J., Guillemot, L., Allen, B., et al. 2012, *ApJ*, **744**, 105
- Price, D. C., 2016 PyGDSM: Python interface to Global Diffuse Sky Models, Astrophysics Source Code Library, ascl:1603.013
- Price, D. C., Flynn, C., & Deller, A. 2021, *PASA*, **38**, e038
- Quintana, A. L., & Wright, N. J. 2021, *MNRAS*, **508**, 2370
- Quintana, A. L., & Wright, N. J. 2022, *MNRAS*, **515**, 687
- Ransom, S., Brazier, A., Chatterjee, S., et al. 2019, *BAAS*, Vol. 51, 195
- Ransom, S. M. 2001, PhD thesis, Harvard University
- Ransom, S. M., Eikenberry, S. S., & Middleditch, J. 2002, *AJ*, **124**, 1788
- Rauw, G., Nazé, Y., Wright, N. J., et al. 2015, *ApJS*, **221**, 1
- Ray, P. S., Kerr, M., Parent, D., et al. 2011, *ApJS*, **194**, 17
- Remazeilles, M., Dickinson, C., Banday, A. J., Bigot-Sazy, M. A., & Ghosh, T. 2015, *MNRAS*, **451**, 4311
- Ridley, J. P., Crawford, F., Lorimer, D. R., et al. 2013, *MNRAS*, **433**, 138
- Roberts, M. S. E., Hessels, J. W. T., Ransom, S. M., et al. 2002, *ApJL*, **577**, L19
- Rygl, K. L. J., Brunthaler, A., Sanna, A., et al. 2012, *A&A*, **539**, A79
- Sanidas, S., Cooper, S., Bassa, C. G., et al. 2019, *A&A*, **626**, A104
- Sayer, R. W., Nice, D. J., & Kaspi, V. M. 1996, *ApJ*, **461**, 357
- Sengar, R., Bailes, M., Balakrishnan, V., et al. 2023, *MNRAS*, **522**, 1071
- Shannon, R. M., Ravi, V., Coles, W. A., et al. 2013, *Sci*, **342**, 334
- Shapiro, I. I. 1966, *PhRv*, **141**, 1219
- Stokes, G. H., Taylor, J. H., Welsberg, J. M., & Dewey, R. J. 1985, *Natur*, **317**, 787
- Stovall, K., Lynch, R. S., Ransom, S. M., et al. 2014, *ApJ*, **791**, 67
- Suryanarayanan, A., Paerels, F., & Leutenegger, M. 2022, arXiv:2212.04165
- Swiggum, J. K., & Gentile, P. A. 2018, *AJ*, **156**, 190
- Swiggum, J. K., Lorimer, D. R., McLaughlin, M. A., et al. 2014, *ApJ*, **787**, 137
- Tauris, T. M., Kramer, M., Freire, P. C. C., et al. 2017, *ApJ*, **846**, 170
- Titus, N., Stappers, B. W., Morello, V., et al. 2019, *MNRAS*, **487**, 4332
- Trepl, L., Hui, C. Y., Cheng, K. S., et al. 2010, *MNRAS*, **405**, 1339
- Trushkin, S. A., Nizhelskij, N. A., Tsybulev, P. G., & Zhekani, G. V. 2017, in *ASP Conf. Ser. 510, Stars: From Collapse to Collapse*, ed. I. I. Romanyuk & I. A. Yakunin (San Francisco, CA: ASP), 492
- Turner, J. E., McLaughlin, M. A., Cordes, J. M., et al. 2021, *ApJ*, **917**, 10
- van der Walt, S. J., Kristensen, L. E., Jørgensen, J. K., et al. 2021, *A&A*, **655**, A86
- van Straten, W., & Bailes, M. 2011, *PASA*, **28**, 1
- Venkatraman Krishnan, V., Flynn, C., Farah, W., et al. 2020, *MNRAS*, **492**, 4752
- Verbiest, J. P. W., Bailes, M., Coles, W. A., et al. 2009, *MNRAS*, **400**, 951
- Vergely, J. L., Lallement, R., & Cox, N. L. J. 2022, *A&A*, **664**, A174
- Virtanen, P., Gommers, R., Oliphant, T. E., et al. 2020, *NatMe*, **17**, 261
- Wahl, H. M., McLaughlin, M. A., Gentile, P. A., et al. 2022, *ApJ*, **926**, 168
- Yao, J. M., Manchester, R. N., & Wang, N. 2017, *ApJ*, **835**, 29
- Yu, Q.-Y., Pan, Z.-C., Qian, L., et al. 2020, *RAA*, **20**, 091
- Zhou, D. J., Han, J. L., Xu, J., et al. 2023, *RAA*, **23**, 104001